



ANNUAL
REVIEWS **Further**

Click [here](#) to view this article's online features:

- Download figures as PPT slides
- Navigate linked references
- Download citations
- Explore related articles
- Search keywords

Accretion onto Pre-Main-Sequence Stars

Lee Hartmann,¹ Gregory Herczeg,²
and Nuria Calvet¹

¹Department of Astronomy, University of Michigan, Ann Arbor, Michigan 48109; email: lhartm@umich.edu, ncalvet@umich.edu

²Kavli Institute for Astronomy and Astrophysics, Peking University, Beijing 100871, People's Republic of China; email: gherczeg1@gmail.com

Annu. Rev. Astron. Astrophys. 2016. 54:135–80

The *Annual Review of Astronomy and Astrophysics* is online at astro.annualreviews.org

This article's doi:

10.1146/annurev-astro-081915-023347

Copyright © 2016 by Annual Reviews.

All rights reserved

Keywords

star formation, accretion disks, pre-main-sequence stars, protoplanetary disks

Abstract

Accretion through circumstellar disks plays an important role in star formation and in establishing the properties of the regions in which planets form and migrate. The mechanisms by which protostellar and protoplanetary disks accrete onto low-mass stars are not clear; angular momentum transport by magnetic fields is thought to be involved, but the low-ionization conditions in major regions of protoplanetary disks lead to a variety of complex nonideal magnetohydrodynamic effects whose implications are not fully understood. Accretion in pre-main-sequence stars of masses $\lesssim 1 M_{\odot}$ (and in at least some $2\text{--}3\text{-}M_{\odot}$ systems) is generally funneled by the stellar magnetic field, which disrupts the disk at scales typically of order a few stellar radii. Matter moving at near free-fall velocities shocks at the stellar surface; the resulting accretion luminosities from the dissipation of kinetic energy indicate that mass addition during the T Tauri phase over the typical disk lifetime ~ 3 Myr is modest in terms of stellar evolution, but is comparable to total disk reservoirs as estimated from millimeter-wave dust emission ($\sim 10^{-2} M_{\odot}$). Pre-main-sequence accretion is not steady, encompassing timescales ranging from approximately hours to a century, with longer-timescale variations tending to be the largest. Accretion during the protostellar phase—while the protostellar envelope is still falling onto the disk—is much less well understood, mostly because the properties of the central obscured protostar are difficult to estimate. Kinematic measurements of protostellar masses with new interferometric facilities should improve estimates of accretion rates during the earliest phases of star formation.

Contents

1. INTRODUCTION	136
2. PRE-MAIN-SEQUENCE MAGNETOSPHERIC ACCRETION	137
2.1. Overview	137
2.2. Magnetospheric Infall and Accretion Shocks	138
2.3. Diagnostics of Accretion Shocks, Inflows, and Outflows	143
2.4. Characteristics of Accretion in Pre-Main-Sequence Stars	151
2.5. Variable Accretion Flows	155
2.6. Accretion in Intermediate-Mass Stars	161
3. THEORIES OF ANGULAR MOMENTUM AND MASS TRANSPORT	162
3.1. Magnetic Instabilities in Nonideal Magnetohydrodynamics	162
3.2. Disk Winds	163
3.3. Hall Effect	164
3.4. Gravitational Instability	165
4. PROTOSTELLAR INFALL AND ACCRETION	165
4.1. Observational Estimates of Protostellar Luminosities and Lifetimes	165
4.2. The Luminosity Problem	167
4.3. Direct Estimates of Protostellar Accretion Rates	169
4.4. Effects of Accretion on Protostellar Properties and Pre-Main-Sequence Stellar Ages	170
4.5. Implications for Planet Formation and Migration	172

1. INTRODUCTION

Stars form through the gravitational collapse of cold interstellar clouds. Although the amount of angular momentum carried away by magnetic fields as infall proceeds is a matter of debate (Li et al. 2014), the vast difference in size between protostars and their natal cloud cores should ensure that much, if not most, of the mass of the final star must be accreted from a rotationally supported disk. Circumstellar disks are detected around many young stars, as needed to explain the high frequency of exoplanets. Thus, the story of star and planet formation is inextricably linked to the processes of disk accretion.

Pre-main-sequence stars exhibit many features of disk accretion in common with other astrophysical objects, such as jets and magnetospheric funneling of mass. Unfortunately, the magnetorotational instability thought to be responsible for turbulent transport in ionized disks is probably of limited relevance for cold, low-ionization protostellar and protoplanetary disks. Although there have been significant recent developments in simulating angular momentum transport with nonideal magnetohydrodynamic effects, our understanding of pre-main-sequence disk accretion remains uncertain. Gravitational instability (GI) may be important in transporting angular momentum in massive young protostellar disks, but this mechanism is unlikely to be relevant at later evolutionary stages.

The main phase of stellar accretion is difficult to study because most protostars are highly extinguished at optical and near-IR wavelengths by the dusty clouds that form them. We therefore begin consideration of pre-main-sequence mass accretion by concentrating on the later stages, when the protostellar envelope has already fallen in or has otherwise been dispersed, and before disk dispersal by planet formation or other mechanisms. We then build on this foundation to

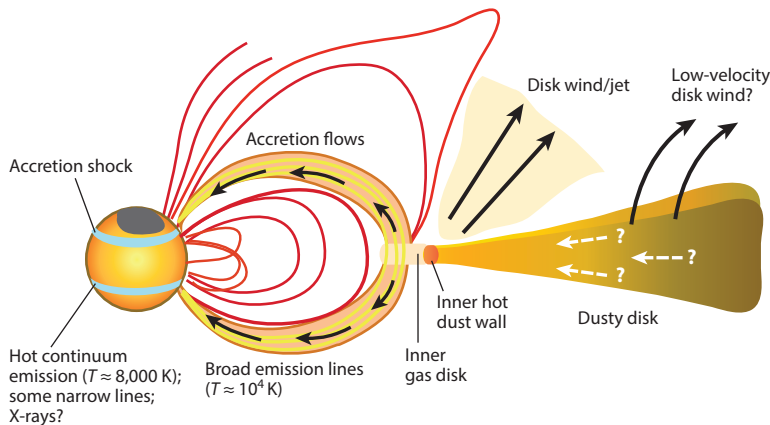


Figure 1

Schematic view of a young star accreting from a disk through the stellar magnetosphere. The strong stellar magnetic field produces large starspots and truncates the disk at a few stellar radii. Magnetic field lines connected with the disk channel material at near free-fall velocities that then shocks at the stellar surface; other magnetic field lines unconnected with the disk produce coronal X-ray emission and/or (unobserved) stellar wind. Some field lines may become twisted by differential rotation between disk and star, causing field lines to bulge out or even eject matter. The inner disk ($\lesssim 1$ AU) produces a bipolar flow or jet, driven by accretion energy; a wind may also be needed to drive disk accretion at larger radii. In general, the mechanisms for transporting mass and angular momentum throughout the disk are uncertain.

address the less-well understood accretion in the protostellar phase. Our discussion focuses on stars of masses $\lesssim 5 M_{\odot}$; higher-mass stars probably also accrete from disks at early times, but much less is known about such accretion, and we do not address this topic here.

2. PRE-MAIN-SEQUENCE MAGNETOSPHERIC ACCRETION

2.1. Overview

Figure 1 shows a schematic view of our current picture of magnetospheric accretion onto young ($1 \lesssim t \lesssim 10$ Myr) low-mass ($\lesssim 1 M_{\odot}$) stars. Material from a circumstellar disk of dust and gas is transported inward by some mechanism (Section 3) to the vicinity of ~ 0.1 AU. Interior to this radius, disk temperatures rise above $\sim 1,000$ K due to heating by the radiation field of the central star, and the dust begins to sublimate; at this dust destruction radius, the inner edge of this dust wall reradiates the energy it absorbs, accounting for much of the observed near-IR excesses. The accretion disk is then truncated by the stellar magnetosphere at a few stellar radii. Matter accretes onto the star, guided by the magnetic field lines in accretion columns or funnel flows. The gas in these columns is heated to temperatures of $\sim 8,000$ K or above by some unknown but presumably magnetic mechanism, producing the observed broad emission lines. The infalling gas moves at essentially free-fall velocities of order $300 \text{ km} \cdot \text{s}^{-1}$ by the time it shocks near the stellar photosphere. The resulting shock heats the gas briefly to temperatures of order 10^6 K; most of the resulting X-ray emission is absorbed and reradiated at lower temperatures, producing strong ultraviolet-optical continuum excesses along with some relatively narrow emission lines (Section 2.2; see also the sidebar *Accretion Versus Stellar Magnetic Activity*).

Emission from the shock is thought to explain the excess continuum fluxes relative to the photospheres observed in young stars. This excess is especially conspicuous at ultraviolet wavelengths,

ACCRETION VERSUS STELLAR MAGNETIC ACTIVITY

Extreme solar-type magnetic activity was offered as an early explanation for the strong emission lines and continua of the low-mass, pre-main-sequence T Tauri stars (TTS). Although TTS do have strong magnetic fields, large starspots, and enhanced chromospheric and coronal emission lines and continua, the very large excesses of many stars are due to the energy released by accretion of external mass. This was clearly demonstrated by the recognition of the so-called weak T Tauri stars (WTTS), many of which have the same ages as the classical T Tauri stars (CTTS), but which have much reduced excess emission, consistent with stellar magnetic activity. Crucially, the WTTS show neither the near-IR excesses observed in the CTTS nor emission from inner-disk gas; this links the CTTS phenomenon to the presence of an inner circumstellar (dusty) disk, the source of the accreted mass. The existence of stars with line and continuum luminosities in excess of photospheric luminosities essentially rules out stellar magnetic activity as the dominant source of energy release in CTTS.

where the observed fluxes can be orders of magnitude higher than the late-type photospheric fluxes in T Tauri stars. At optical and near-IR wavelengths, the excess adds to the photospheric fluxes, making the absorption lines appear less deep than in nonaccreting stars; this phenomenon is called veiling (Section 2.3).

This picture assumes that the stellar magnetic field is sufficiently strong, and the pressure of the accretion disk sufficiently limited, that the disk is disrupted before it reaches the star. Observations of accreting pre-main-sequence stars with masses $\lesssim 1 M_{\odot}$ are consistent with magnetospheric accretion, extending down to the brown dwarf regime. However, magnetospheric accretion may not occur for other stars, especially at intermediate ($2\text{--}5\text{-}M_{\odot}$) and higher masses (Section 2.6), when magnetic fields are weak. It also appears not to apply for a few systems that have very high rates of accretion during outbursts (FU Ori objects; see Section 2.5.3), during which the emission lines formed in the magnetospheric accretion columns disappear, presumably because the disk crushes the field back to the star.

2.2. Magnetospheric Infall and Accretion Shocks

A sufficiently strong stellar magnetic field can truncate an accretion disk at a point where magnetic and gas ram pressures roughly balance, $B^2/8\pi \approx \rho v^2$, and where the relevant velocity is approximately the Keplerian value. Making the usual approximation of a dipole field of strength B_{\circ} at the stellar radius R_{\ast} , the magnetospheric radius becomes

$$r_{\text{M}} \approx \xi \left(\frac{\mu^4}{4GM_{\ast}\dot{M}^2} \right)^{1/7} \approx 18\xi \frac{B_3^{4/7} R_2^{12/7}}{M_{0.5}^{1/7} \dot{M}_{-8}^{2/7}} R_{\odot}, \quad (1)$$

where μ is the dipole moment of the star and $\xi \lesssim 1$ is a correction factor dependent upon the details of the disk-magnetosphere interaction. We use fiducial numbers $M_{\ast} = 0.5 M_{\odot}$ and $R_{\ast} = 2 R_{\odot}$, a typical accretion rate $\dot{M} = 10^{-8} M_{\odot} \cdot \text{year}^{-1}$, and a magnetic field of $B_3 = 1$ kG. Adopting values of $\xi \approx 0.7$ and $B \approx 1\text{--}2$ kG, we have $r_{\text{M}} \approx 4\text{--}6 R_{\ast}$.

For matter to fall in toward the star, it must lose angular momentum, and so the magnetic field lines channeling the flow must connect to regions of the disk inside of the corotation radius R_{co} . This process transfers angular momentum to the star. However, many T Tauri stars, especially those with inner disks, are slow rotators, indicating that there must be significant angular momentum loss to compensate for this spinup by accretion. The Keplerian period at the above fiducial

radius is $\sim 4\text{--}7$ days, comparable to typical stellar rotation periods (see the review by Bouvier et al. 2014); this has led to the suggestion that some stellar magnetic field lines couple to the disk outside of R_{co} to prevent stellar spinup (e.g., Königl 1991). The disk must then transfer the necessary angular momentum outward either internally or via a wind; stellar winds may also play a role in spindown. A discussion of possible disk regulation of stellar spin is beyond the scope of this review; here we simply make the assumption that the truncation radius is not far inside corotation, and so for present purposes we adopt a fiducial value $r_{\text{M}} \approx R_{\text{co}} \approx 5.5 R_*$, corresponding to a stellar rotation period of 6 days.

With truncation of the disk at several stellar radii, the accreting matter will fall at near free-fall velocities from r_{M} , resulting in an accretion shock at the stellar surface that radiates away the kinetic energy. Numerically,

$$v_{\text{ff}} = \left(\frac{2GM_*}{R_*} \right)^{1/2} \left(1 - \frac{R_*}{R_{\text{M}}} \right)^{1/2} \approx 280 M_{0.5}^{1/2} R_2^{-1/2} \text{ km} \cdot \text{s}^{-1}, \quad (2)$$

where $M_{0.5}$ and R_2 are the stellar mass and radius in units of $0.5 M_{\odot}$ and $2 R_{\odot}$, and we assume $R_{\text{co}} \approx 6R_*$. The accretion shock luminosity, assuming complete dissipation of the kinetic energy, is

$$L_s = \frac{1}{2} \dot{M} v_{\text{ff}}^2 = \frac{GM_* \dot{M}}{R_*} \left(1 - \frac{R_*}{R_{\text{M}}} \right) \approx 0.8 \frac{GM_* \dot{M}}{R_*}, \quad (3)$$

where \dot{M} is the rate of mass accretion onto the star. Thus, as long as the truncation radius is at several stellar radii, measuring the accretion shock luminosity provides a reasonable estimate of the mass accretion rate, given known stellar parameters.

Using the strong-shock approximation, which is appropriate given the high Mach number of the flow, the temperature of the shock, setting $v_s = v_{\text{ff}}$, is

$$T_s = \frac{3}{16} \frac{\mu m_{\text{H}}}{k} v_s^2 = 8.8 \times 10^5 M_{0.5} R_2^{-1} \text{ K}, \quad (4)$$

so radiation from the shock produces soft X-rays that irradiate the medium surrounding it. The absorbed portion of this radiation is reprocessed into longer wavelengths and eventually emitted, producing excess emission over the intrinsically photospheric flux.

To model the emission from the shock region, it is usually assumed that the shock is plane-parallel and vertical, which is justified by its small extent, and that the emitting region is in a vertical column constrained by the magnetic field. The density of the incoming material is $\rho = \dot{M}/Av_s$, where A is the area covered by accretion columns, which can be expressed in terms of a filling factor f as $A = f4\pi R_*^2$. Then the total number density is

$$n \approx 7 \times 10^{12} \dot{M}_{-5} M_{0.5}^{-1/2} R_2^{-3/2} f_{0.01}^{-1} \text{ cm}^{-3}, \quad (5)$$

where $f_{0.01}$ is the fraction of the stellar surface covered by the accretion columns in units of percent. The ram pressure of this material is $p_{\text{ram}} = \rho v_p^2$, or

$$p_{\text{ram}} \approx 1.2 \times 10^4 \dot{M}_{-8} M_{0.5}^{1/2} R_2^{-5/2} f_{0.01}^{-1} \text{ dyn} \cdot \text{cm}^{-2}. \quad (6)$$

The stellar photospheric pressure at the depth of continuum formation is on the order of $p_{\text{ph}} \approx 2/3 g/\chi_R$, which, for gravity $\log g \approx 3.5$ (cgs) and Rosseland mean opacity $\chi_R \approx 10^{-2} \text{ cm}^2 \cdot \text{g}^{-1}$ [values appropriate to atmospheric densities and effective temperatures ($\sim 3,600$ K) of a $0.5\text{-}M_{\odot}$ T Tauri star], corresponds to $\sim 10^4 \text{ dyn} \cdot \text{cm}^{-2}$, indicating that the shock forms near the photosphere (Calvet & Gullbring 1998). As long as the energy flux is not very large ($\log \mathcal{F} < 12$), essentially all of the accretion luminosity should be radiated away (Section 4).

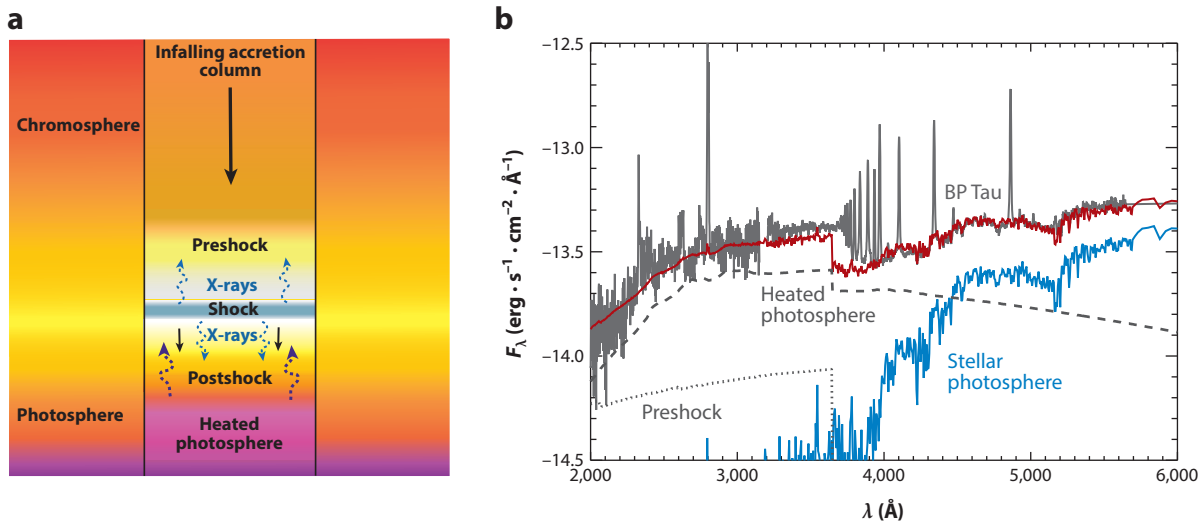


Figure 2

(a) Schematic diagram of accretion shock structure showing the precursor or preshock region, the postshock or cooling region, and the heated photosphere below the shock. (b) Spectral energy distribution of the classical T Tauri star BP Tau (*gray solid line*), stellar photosphere (*blue line*), and accretion shock model (*red line*) showing contributions from the preshock (*gray dotted line*) and heated photosphere–postshock (*gray dashed line*) regions. Shock model courtesy of L. Ingleby.

The structure and continuum emission of the accretion shock region can be estimated from simple physical principles. The column is generally divided into three subregions shown schematically in **Figure 2a**: the precursor or preshock region, the postshock or cooling region, and the heated photosphere below the shock (Stahler et al. 1980; Lamzin 1995a, 1998; Calvet & Gullbring 1998; Gullbring et al. 2000; Günther et al. 2007b). The shock emits $\frac{1}{2}$ of its energy downward into the postshock region and photosphere and $\frac{1}{2}$ upward into the preshock region, which reprocesses this energy, sending back down $\sim\frac{1}{2}$ of it. The heated photosphere is then irradiated with $\sim\frac{3}{4}$ of the shock energy, reprocesses it into longer wavelengths, and emits it upward. With no significant absorption in the cooling region, the energy emerging from the region is then $\sim\frac{1}{4}$ of the shock energy from the preshock region plus $\sim\frac{3}{4}$ of the energy from the heated photosphere and postshock region (Lamzin 1995a, 1998; Calvet & Gullbring 1998).

Matter heated to temperatures given by Equation 4 cools down, decelerates, and gets denser in the postshock region. The thickness of this region, subject to radiative cooling in X-rays and ultraviolet lines, can be estimated as $l_{\text{post}} = v_{\text{post}} t_{\text{rad}}$, with $v_{\text{post}} = \frac{1}{4} v_s$ and with cooling time $t_{\text{rad}} = 6.7 \times 10^3 T^{3/2} / n_e$ s, which is appropriate for optically thin cooling (Sacco et al. 2008). With the electron density n_e equal to 4 times the density of the preshock region, we obtain

$$l_{\text{post}} = 7 \times 10^5 \dot{M}_{-8}^{-1} M_{0.5}^{5/4} R_2^{-1/2} f_{0.01} \text{ cm}, \quad (7)$$

much smaller than the stellar radius, justifying the plane-parallel approximation. The postshock gas merges into the star through a region akin to the stellar photosphere but significantly altered by being heated from above by $\sim\frac{3}{4}$ of the shock energy. We can estimate its emission by assuming that its effective temperature is given by $\sim(3\mathcal{F}/4\sigma)^{1/4}$, where \mathcal{F} is the energy flux carried by the column,

$$\mathcal{F} = \frac{1}{2} \rho v_s^3 \approx 1.7 \times 10^{11} \dot{M}_{-8} M_{0.5} R_2^{-3} f_{0.01}^{-1} \text{ erg} \cdot \text{cm}^{-2} \cdot \text{s}^{-1}, \quad (8)$$

for the fiducial parameters. The effective temperature of the heated photosphere for this flux is

$$T_{\text{hp}} \sim 7,420 \text{ K } \dot{M}_{-8}^{1/4} M_{0.5}^{1/4} R_2^{-3/4} f_{0.01}^{-1/4}. \quad (9)$$

The preshock region absorbs $\frac{1}{2}$ of the soft X-rays emitted by the shock. Assuming that all the radiation is below the H ionization threshold, the size of the preshock region can be estimated by equating the number of ionizing photons to the number of recombinations, $\frac{1}{2}\mathcal{F}/E_\gamma = \rho v_s^3/4E_\gamma = n_e^2 \alpha_{\text{H}} l_{\text{pre}}$, where E_γ is the average energy of the incoming photons, n_e is the electron density, α_{H} is the recombination coefficient, and l_{pre} is the vertical extent of the region (Lamzin 1995b). Using Equations 8, 2, and 5, the size of the preshock region is

$$l_{\text{pre}} \approx 7.6 \times 10^7 \dot{M}_{-8}^{-1} M_{0.5}^2 f_{0.01} \text{ cm}, \quad (10)$$

much smaller than the stellar radius. Collisional excitation keeps the temperature of this optically thin region at $\sim 10^4$ K, so its spectrum is essentially that of a (high-density) HII region (Lamzin 1995b, 2003).

Calvet & Gullbring (1998) calculated the emission from this type of shock model, characterizing the plane-parallel, uniform columns by an energy flux \mathcal{F} and a filling factor f . These models adopted a one-fluid calculation of the structure of the postshock region, which was matched to the hydrostatic structure of the photosphere below irradiated by the shock. The temperature of the heated photosphere, calculated with a two-wavelength treatment based on mean opacities, was higher than that of the surrounding photosphere at the same optical depth, with temperatures at the depth of continuum formation of the order of Equation 9, falling to a minimum at $\tau_{\text{cont}} \approx 10^{-2} - 10^{-3}$ and then rising sharply toward the shock.

The emission of the region was calculated assuming local thermodynamic equilibrium and using the appropriate opacity sources, including line blanketing. **Figure 2b** shows the spectrum of a classical T Tauri star (CTTS) together with a shock model, indicating separately the emission of each region. The heated photosphere peaks at shorter wavelengths than the stellar photosphere because of its higher temperature (Equation 9). A contribution to the Balmer jump arises in the transition region, where the photosphere joins the postshock region. The optically thin preshock region adds to the continuum emission mostly at the Balmer jump and in the far-ultraviolet (FUV) region (**Figure 2**). Despite its simplicity, this model reproduces the observed continuum excesses in the blue and the ultraviolet spectra of low-mass and intermediate-mass T Tauri stars, brown dwarfs, and some Herbig Ae/Be (HAeBe) stars reasonably well (Calvet & Gullbring 1998; Gullbring et al. 2000; Ardila & Basri 2000; Muzerolle et al. 2000, 2003; Calvet 2004; Muzerolle et al. 2004; Mendigutia et al. 2011). Values of \mathcal{F} are estimated from the spectral shape of the excess continuum, and of f from the absolute value of the excess; typical values are $\log \mathcal{F} \approx 10.5 - 11.5$, consistent with expectations (Equation 8), and $f \approx 0.001 - 0.01$. The small covering factors support the modeling of emergent spectra as the sum of accretion shock emission plus a relatively undisturbed stellar photospheric spectrum (Section 2.4).

The idealized concept of homogeneous accretion columns is consistent with matter infall along a dipolar magnetic field, as sketched in **Figure 1**. However, the accretion flows are obviously much more complex. Actual accretion flows are not homogeneous in density or in temperature, so as a first approximation they could be explained as a superposition of accretion columns. Moreover, solar-mass T Tauri stars have surface-averaged magnetic field strengths of 1–2 kG (e.g., Johns-Krull 2007, Donati & Landstreet 2009), which is sufficient to produce magnetospheric truncation radii near corotation if the field were purely dipolar (Equation 1). However, much of the field is distributed in quadrupolar and higher-order moments, including small-scale fields that cover the entire stellar surface (Donati et al. 2008, Chen & Johns-Krull 2013), implying that the dipolar component is considerably weaker. In Zeeman–Doppler imaging, measurements

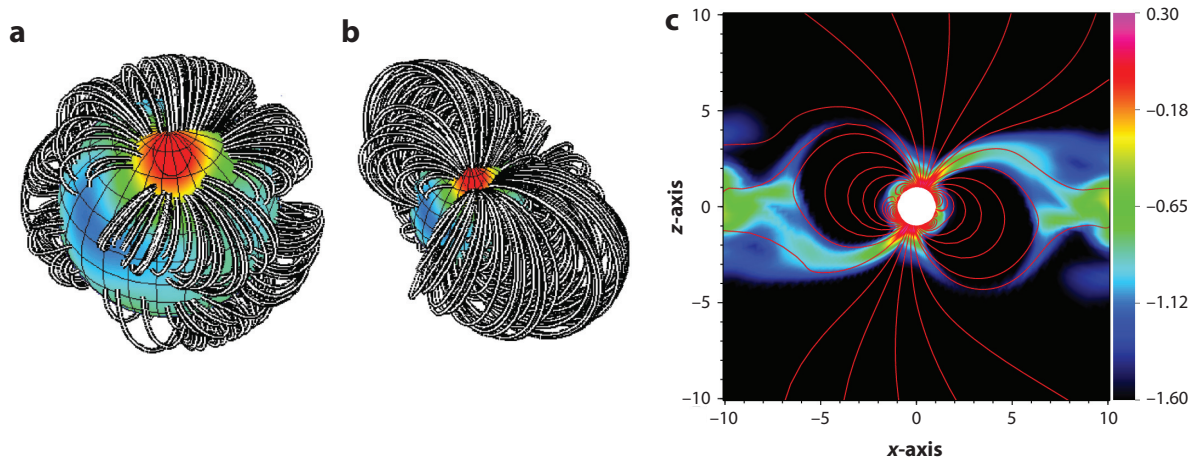


Figure 3

Magnetic field morphology of V2129 Oph, showing (a) complex high-order fields and (b) a large-scale, dipole-like magnetic field (Donati et al. 2007, Gregory et al. 2008). The large-scale field is tilted by $\sim 20^\circ$ from the disk, which leads to formation of a funnel flow that connects to the star near the pole. (c) A slice of the density in the accretion flow of V2129 Oph from Alencar et al. (2012), based on simulations by Romanova et al. (2011) of how matter would flow along the magnetic field lines. Magnetic field figures courtesy of J.-F. Donati, S. Gregory, and M. Jardine.

of rotational modulation of the polarization of photospheric lines and in the narrow components of emission lines have been used to reconstruct the large-scale topology of the magnetic field and the distribution of accretion spots. These techniques reveal magnetic fields with strong multipolar components and distributions of spots inhomogeneous in latitude and longitude, with preference toward the magnetic poles (see Donati et al. 2008).

As an example, **Figure 3** shows the reconstructed magnetic field of V2129 Oph, indicating separately the complex 1.2-kG octupolar surface field and the 0.35-kG dipolar large-scale field, the latter tilted relative to the stellar rotation axis by 20° (Donati et al. 2007, Gregory et al. 2008). In these magnetic field maps, the quadrupolar fields are assumed to be negligible because their presence would channel the accretion flow to equatorial locations on the star, in contrast to the detections of polar accretion spots. The weaker dipole fields found in Zeeman–Doppler imaging campaigns lead to smaller truncation radii than if the total magnetic flux is used (Bessolaz et al. 2008, Johnstone et al. 2014). However, the dipole field strengths of dark spots may be underestimated, depending on whether the surface filling factor is considered (Chen & Johns-Krull 2013) or if magnetic flux cancellation is important (see the review by Hussain & Alecian 2014). In any case, a truncation radius near or inside corotation is consistent with the structure of the inner disk (see the review by Dullemond & Monnier 2010), including the inner radius of CO emission (Najita et al. 2003, Salyk et al. 2011). These truncation radii are also consistent with the location of extinction events, which are caused by disk warps associated with accretion along inclined dipoles (e.g., Bouvier et al. 2007, McGinnis et al. 2015) and have periods that are roughly consistent with corotation.

Magnetohydrodynamic (MHD) simulations in two and three dimensions of the accretion flows in rotating stars with tilted dipolar fields predict that matter flows toward the star in two funnels for high tilt angle and in multiple funnels for low tilt angle. The distribution of hot spots, spot covering area, and distribution of spot temperature and density all depend on the tilt angle and

mass accretion rate, with an inverse correlation between spot density and the filling factor of each density [see Romanova et al. (2014) and references therein]. Models with more complex magnetic field morphology based on observational reconstructions (e.g., **Figure 3**) indicate that the gas initially flows along the dipole field lines, in some cases in well-ordered funnel flows in a stable accretion regime (e.g., Bouvier et al. 2007, Kurosawa & Romanova 2013). Near the stellar surface, strong octupolar fields alter the flow of material. The flow footpoint is located at high latitudes on the star when dipolar and octupolar fields dominate and at mid-latitudes when quadrupolar or higher-order fields dominate (Romanova et al. 2011, 2014 and references therein; Adams & Gregory 2012; Johnstone et al. 2014).

In a series of studies, researchers have analyzed the time evolution of the accretion shock (Sacco et al. 2008, 2010; Orlando et al. 2010; Bonito et al. 2014, and references therein). In these studies, the flow and shock are calculated from gravity stratification, radiative cooling, and thermal conduction in 1D and 2D geometries, although at much lower densities than expected for T Tauri shocks. When the magnetic field strongly constrains the flow, the postshock thickness oscillates, owing to a radiative shock instability, with a period of 0.1–1 s that depends on the density and velocity of the stream. The oscillations have not been observed (Günther et al. 2010); if the accretion stream is inhomogeneous, as suggested by 3D simulation (Romanova et al. 2004), these oscillations would be difficult to detect (Sacco et al. 2010).

2.3. Diagnostics of Accretion Shocks, Inflows, and Outflows

The emission associated with the release of accretion energy arises from a wide variety of environments with differing temperatures and densities. As discussed in Section 2.2, in the vicinity of the accretion shock, the temperature and density vary on small scales. The shock produces near-ultraviolet (NUV), optical, and near-IR continua, which constitute most of the radiative losses associated with dissipation of the accretion energy, along with a small amount of X-ray emission. Some emission lines are also produced in the shock region; however, many of the strongest optical lines characteristic of T Tauri stars (e.g., the Balmer series) are formed in the extended magnetospheric infall region (**Figure 1**). The line profiles of various species are crucial to disentangling the region(s) of their formation. Lines with large widths comparable to the free-fall velocity arise in the extended magnetosphere, whereas narrow lines are more likely produced in the region of the accretion shock. In addition, lines formed in accretion-driven winds and/or stellar winds probe regions beyond the magnetosphere. In Section 2.3.1, we consider emissions arising from the various regions of accretion flow and their diagnostic lines and continua.

2.3.1. The accretion shock. The shock emission serves as a probe of the structure of the accretion shock region, with a luminosity that is the necessary input for estimates of mass accretion rate (Section 2.4). A typical CTTS spectrum includes line and continuum emission from the accretion flow and shock, mixed with emission from chromospheric activity and the stellar photosphere. To analyze the accretion flow and shock, the excess emission is extracted from the observed flux by subtracting the stellar photospheric flux; this excess is then attributed to some component of the accretion flow. The excess can be measured directly at ultraviolet wavelengths in CTTS because of the diminished flux from the cool photosphere, although for the mostly slowly accreting stars, the stellar chromosphere may hide the accretion emission (Ingleby et al. 2011; see also **Figure 2b**). In the optical wavelength region, the excess emission is extracted from the observed spectrum by measuring the veiling of the absorption lines, i.e., the degree to which the line to continuum ratio

decreases by the addition of flux to the stellar emission. The spectral shape of the excess is then compared to that predicted by models to determine the structure of the emitting region.

In the shock models that have been explored in the literature (Lamzin 1998, Calvet & Gullbring 1998; see also Section 2.2), radiation from the heated photosphere escapes along the hotter regions of the accretion column because these regions are intrinsically transparent in the NUV and longer wavelengths. These uniform shock models do a reasonably good job of explaining the excess emission in the ultraviolet range (see **Figure 2b**). However, they predict fluxes at red-optical wavelengths that are lower than observed in veiling measurements (e.g., Fischer et al. 2011, McClure et al. 2013). This difficulty is overcome by invoking the presence of multiple accretion flows with different densities, and therefore different values of the energy flux \mathcal{F} (Ingleby et al. 2013), as expected from simulations based on actual magnetic field structures (Section 2.2). The higher-density (10^{11} – 10^{12} cm $^{-3}$) spots cover approximately 0.1–1% of the stellar surface, whereas the lower-density (10^{10} – 10^{11} cm $^{-3}$) and therefore cooler spots cover 0–40% of the surface. These sizes are roughly consistent with the measured sizes of accretion hot spots of a few percent measured from Zeeman–Doppler imaging (e.g., Donati et al. 2011). Mass carried by cold columns is comparable to that carried by hot columns, implying an intrinsic uncertainty in L_{acc} and \dot{M} determinations from the fact that emission from cool columns can be hidden below the photosphere in the weak accretors (Section 2.4.1).

Additional observational diagnostics that constrain shock models include the total luminosity (see also the discussion in Section 2.4.1), the flux ratios of the different continuum spectra (including the Balmer jump—other ionization edges are weaker and difficult to detect), and the spectral shape, especially at red and ultraviolet wavelengths. The observed Balmer jumps are typically factors of 1.5–3, although in extreme cases they may be as high as 15 if optically thin emission dominates or as low as 1 if the emission is produced in optically thick regions (e.g., Valenti et al. 1993, Gullbring et al. 1998, Herczeg et al. 2009, Rigliaco et al. 2012, Alcalá et al. 2014). The size of the Balmer jump tends to be larger for small accretion rates onto very low-mass stars and brown dwarfs, although exceptions to this trend exist. This diversity presents a challenge for shock models, which produced Balmer jumps between 1.1–1.7 (Calvet & Gullbring 1998). Ingleby et al. (2014) suggest that some accretion flows may have a large volume of preshock gas, which produces optically thin emission and would therefore yield larger values for the Balmer jump.

Although most of the X-ray emission from the shock is expected to be absorbed, observations with spectrometers on board the *Chandra X-ray Observatory* (*Chandra*) and the *X-ray Multi-Mirror Mission–Newton* have found soft X-ray emission produced by gas with temperatures $T \approx \text{few} \times 10^6$ K and electron densities $n_e \approx 10^{11}$ – 10^{12} cm $^{-3}$, very different from coronal gas with $T \approx 10^7$ K and $n_e \leq 10^{10}$ cm $^{-3}$. This emission is never observed in nonaccreting stars and likely forms in the postshock region (Kastner et al. 2002, Stelzer & Schmitt 2004, Argiroffi et al. 2007, Günther et al. 2007b, Güdel & Nazé 2010), providing strong support to the magnetospheric accretion model.

Figure 4 shows that the high-resolution *Chandra* spectrum of TW Hya is rich in emission lines, identified with model components produced by the accretion shock and by the stellar corona (Brickhouse et al. 2010). The luminosities of these components are 6.9×10^{29} erg \cdot s $^{-1}$ for the shock and 3.4×10^{30} erg \cdot s $^{-1}$ for the corona. Only $\sim 4\%$ of the total accretion energy from TW Hya escapes as X-rays, as most of this energy is reprocessed into the ultraviolet-optical continuum emission (e.g., Alencar & Batalha 2002, Herczeg & Hillenbrand 2008, Ingleby et al. 2013). The fluxes in forbidden and intercombination lines of the helium-like ions of nitrogen, oxygen, neon, and magnesium have been modeled with accretion column models aiming to determine departures from the single-column model. The sophistication of these models varies from 1D, stationary models with nonequilibrium ionization (Lamzin 1998, Günther et al. 2007b,

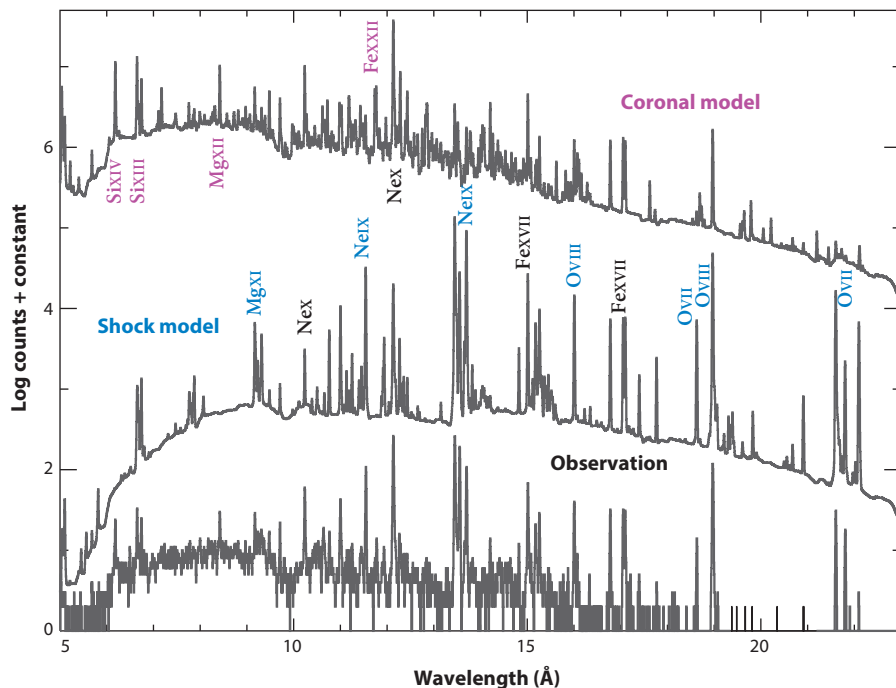


Figure 4

Model components of the observed X-ray spectrum of TW Hya (*bottom*). The model is composed of the shock emission component (*middle*) and a coronal component (*top*). The most studied lines have been labeled, with the purple and blue labels indicating the lines that most clearly distinguish between coronal and shock origins, respectively. Courtesy of N. Brickhouse.

Lamzin 1998, Brickhouse et al. 2010) to 1D and 3D MHD simulations including gravity, thermal conduction, and interaction with surrounding chromospheric material (Sacco et al. 2008, 2010; Bonito et al. 2014). It was realized early that high column densities ($N \approx 10^{24} \text{ cm}^{-2}$) at shock formation (Calvet & Gullbring 1998) would lead to absorption of the X-ray spectrum of the postshock emission (Drake 2005)—the shock would be buried in the atmosphere—although these effects would be mitigated by columns of low density (Sacco et al. 2008, 2010). Detailed calculations of deep high-resolution *Chandra* spectra of TW Hya by Brickhouse et al. (2010, 2012) showed that multiple high-density diagnostics can be fitted, assuming photoelectric absorption in a column consistent with the standard accretion model. Moreover, the mass accretion rates derived from the X-rays, when accounting for absorption, are similar to ultraviolet and optical determinations (Sacco et al. 2010, Brickhouse et al. 2010), eliminating discrepancies found in early treatments (Stelzer & Schmitt 2004, Günther et al. 2007b).

Brickhouse et al. (2010, 2012) found that line ratios of ions such as OVI, NeIX, and MgXI yield densities that are consistent with the standard accretion models. However, lines of OVI indicate densities about five times lower than the NeIX and MgXI triplets, contrary to the expectation of increasing densities as the postshock cools off. Brickhouse et al. proposed that some X-ray emission escapes the shock horizontally into the surrounding photosphere, heating it and supplying the material to nearby magnetic structures in which the OVI lines arise. An alternative explanation has been offered by Bonito et al. (2014), who carried out 3D MHD dynamical simulations of accretion columns immersed in chromospheres. They considered a stream with density decreasing

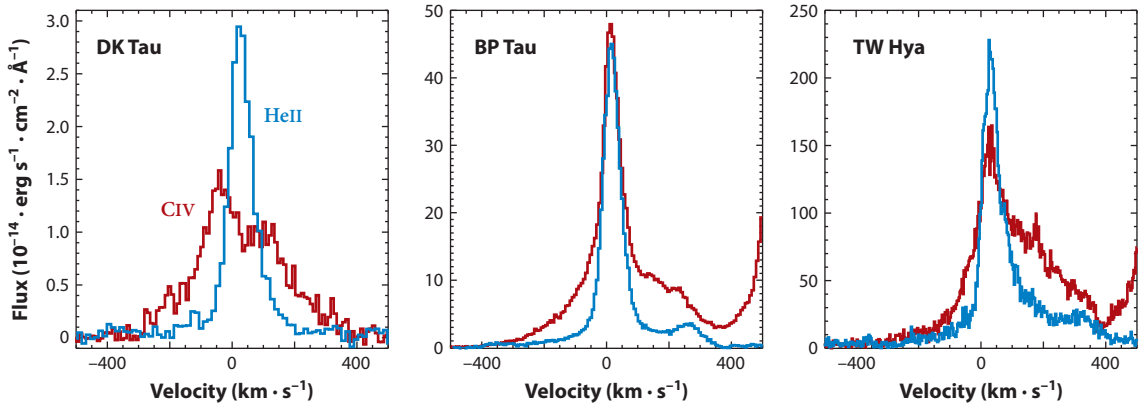


Figure 5

CIV 1,548-Å and HeII 1,640-Å line profiles show narrow components thought to arise in the postshock region as well as broad components that extend to $\sim 400 \text{ km} \cdot \text{s}^{-1}$ from the magnetospheric flow. Adapted from Ardila et al. (2013) with permission.

toward the edge, as obtained by Romanova et al. (2011), and found that the OVII lines, located in the softer part of the X-ray spectrum, were subject to higher absorption. The observed OVII emission would then come mostly from the lower-density, peripheral parts of the column, whereas higher-temperature lines would have a much larger contribution from the denser central parts.

Some ultraviolet lines, such as the CIV resonance doublet and the HeII 1,640-Å, show a broad component (BC) that may form in part of the magnetospheric flow and a narrow component (NC) that is more consistent with formation in the postshock region (Figure 5). NCs are also seen in some optical and near-IR lines such as the CaII triplet, HeI 5,876 Å, and HeII 1,640 Å (Figure 6). The NCs and narrow lines are generally redshifted with respect to the stellar velocities, with larger redshifts corresponding to higher-ionization equilibrium lines (Beristain et al. 2001, Ardila et al. 2013), in agreement with the expected decrease of velocity as lines form in the decelerating, cooler postshock regions. However, the preshock region has been proposed as the site of formation of the intercombination lines [CIII] 1,909 Å, [SIII] 1,892 Å, and [OIII] 1,665 Å on the basis of the density of formation inferred from their fluxes and line ratios (Gómez de Castro & Lamzin 1999).

Spectropolarimetry of the narrow component of the HeII emission line shows that the line is formed in a strongly magnetized region, reaching 6 kG for GQ Tau, which confirms that the narrow component is produced in the region near the base of the accretion flow (e.g., Symington et al. 2005, Yang et al. 2007, Donati et al. 2011, Johns-Krull et al. 2013). Maps of the CaII emission line on the stellar surface indicate that the line emission covers $\sim 10\%$ of the stellar surface, often at or near the poles for dipole–octupole configurations and at lower latitudes when higher-order fields are stronger (e.g., Hussain et al. 2009, Donati et al. 2011). These results match the expectations of the size and location of the accretion region. In general, the flux in the NCs and narrow lines correlates with veiling and the accretion rate (Beristain et al. 2001, Ardila et al. 2013). The same ultraviolet and often optical lines are usually present in weak T Tauri stars (WTTS) with similar widths as the NCs from CTTS, but with smaller redshifts and much fainter luminosities, as expected for stellar chromospheric and transition-region emission. These regions may provide important contributions to emission, especially in slowly accreting stars.

2.3.2. Magnetospheric accretion flows. The large line widths of some emission lines (Figure 6) represent highly supersonic flows; as the maximum velocities seen are roughly

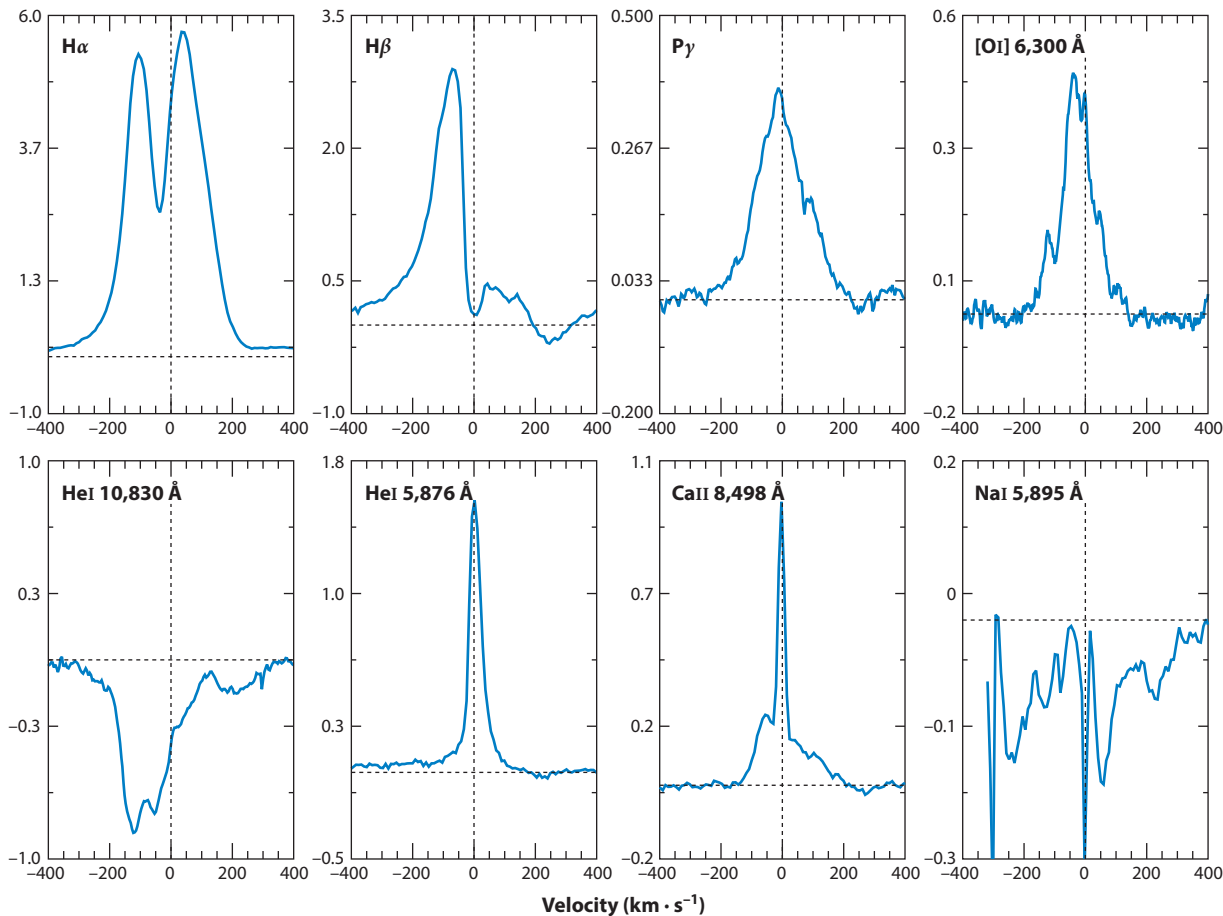


Figure 6

Line profiles of the Classical T Tauri star DK Tau. The strong $H\alpha$ line shows blueshifted wind absorption superimposed upon broad emission. In contrast, the $H\beta$ and Paschen γ ($P\gamma$) lines do not show the blueshifted absorption because of lower optical depth; instead, they exhibit the roughly central emission peak and, along with the Na I resonance doublet, the redshifted absorption typical of models of magnetospheric infall. The [O I] line shows broad blueshifted emission formed in the wind and/or jet. The He I 10,830-Å line shows both blueshifted wind absorption and a redshifted component from infalling material. Finally, the He I 5,876-Å and Ca II IR triplet members show very narrow emission or emission components centered at the stellar velocity, which likely arise from the postshock gas. Thus, differing transitions probe differing regions, depending upon line strength and radiative transfer effects. Courtesy of S. Edwards.

consistent with free-fall velocities (Bonnell et al. 1998), such BCs must form in the magnetosphere. However, interpreting the line profiles in detail has proved difficult because of a combination of complex geometries and radiative transfer effects, as well as winds. The recognition of magnetospheric infall rests on observations of specific lines that show redshifted absorption more clearly (e.g., $H\beta$ and the Na I resonance doublet shown in **Figure 6**), along with sophisticated radiative transfer modeling to explain why other line emissions formed in the magnetosphere, such as $H\alpha$, often do not show signatures of infall (Muzerolle et al. 2001; see also **Figure 6**).

Models assuming free fall along axisymmetric, dipolar magnetic field lines have been successful in explaining line profiles of Balmer lines in CTTS (Hartmann et al. 1994; Muzerolle et al. 1998, 2001), in brown dwarfs (Muzerolle et al. 2000, 2003), and in some Herbig Ae (HAe) stars

(Muzerolle et al. 2004), as well as explaining some He I lines in CTTS (Kurosawa et al. 2011). In these models, the density along streamlines is calculated for a constant infall rate \dot{M} and area consistent with the assumed geometry, starting from zero velocity at the disk. Models including Stark, radiative, and van der Waals broadening show that the line wings can extend beyond the free-fall velocity, especially in high-opacity lines in strong accretors.

One limitation of these models is that the heating of the plasma is not understood, although it is expected to be magnetic in nature. To circumvent this problem, Muzerolle et al. (2001) determine optimal temperature ranges based on comparisons with observations. These models can explain the differences observed among emission lines in terms of optical depth effects. For instance, in rapid accretors such as DR Tau, H α requires emission from an extended region such as the wind, but even in this case lower-opacity lines that form closer to the star have profiles consistent with magnetospheric infall (Muzerolle et al. 2001). Similar analyses of synthetic and observed line profiles have led to a temperature measurement of 9,000 K for the magnetospheric flow of AA Tau (Esau et al. 2014). Ratios of the H Paschen and Brackett series from a larger sample of stars indicate that these lines are formed in regions with densities of $n_{\text{H}} \approx 10^{10}$ – 10^{11} cm $^{-2}$ (Edwards et al. 2013), also consistent with expectations for the magnetospheric flow.

Numerical calculations with more complex and realistic magnetic field geometries consistent with MHD simulations of Romanova et al. (2012) similarly predict profiles consistent with observations (Kurosawa & Romanova 2012, Alencar et al. 2012). As an illustration, **Figure 7** shows H β line profiles for the CTTS V2129 Oph, modeled by calculating the emission of structures based on MHD simulations of how accretion flows through the magnetic field structure, as mapped with Zeeman–Doppler imaging (Donati et al. 2011, Kurosawa et al. 2011, Romanova et al. 2011, Alencar et al. 2012). The emission line map (**Figure 7a**) shows that the emission is produced

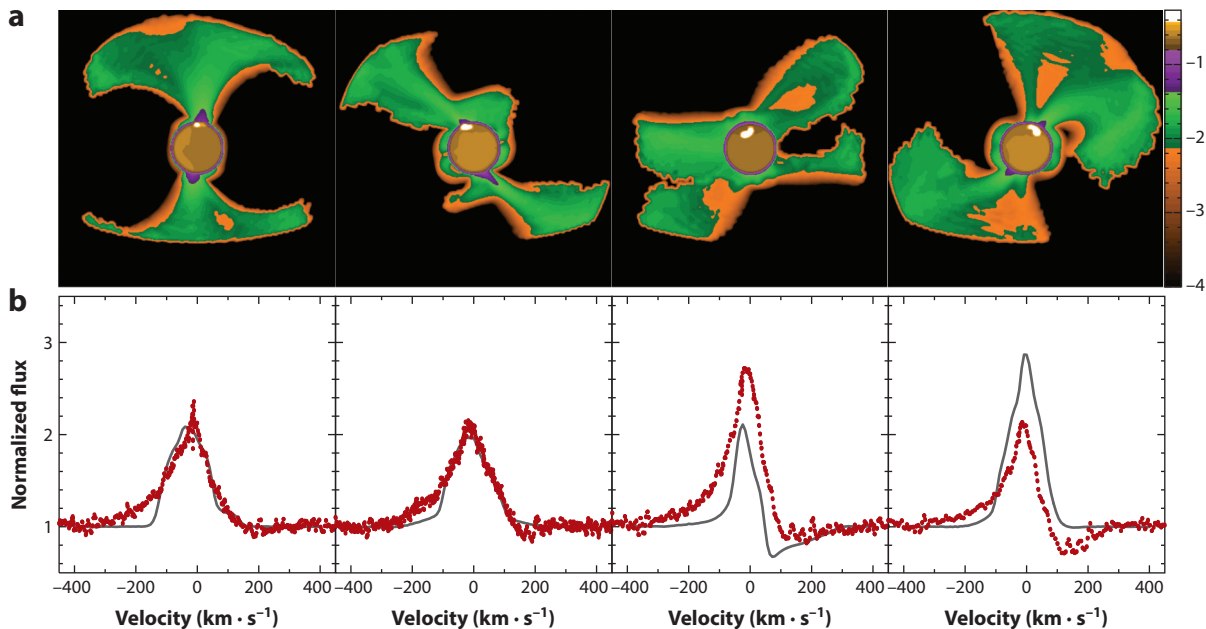


Figure 7

(a) H β emission line maps and (b) profiles (gray line, model; red dots, observed) at four phases of the rotation period. (a) The maps are calculated from the magnetic field maps and accretion models generated in **Figure 3**. Adapted from Alencar et al. (2012) with permission.

in the magnetospheric accretion columns. The model profiles agree well with the measured line profile shapes obtained at different rotational phases. In this example, accretion in a complex field geometry results in an observable redshifted component at only some phases, depending upon the viewing angle. The presence of redshifted absorption features is sensitive to the topology of the accretion flow and our line of sight (e.g., Kurosawa et al. 2011); any flows to the stellar equator, as expected in some unsteady accretion regimes (Blinova et al. 2016), would only rarely produce redshifted absorption.

In addition to geometry, radiative transfer effects are important for whether a line formed in the magnetosphere exhibits redshifted absorption. For example, such absorption components in H α are rare in stars with high mass accretion rates (Fischer et al. 2008), but can be obvious in the slowest accretors (Ingleby et al. 2013). These trends can be understood in terms of optical depth effects. High-opacity lines like H α are thermalized even in the wings in high-density flows, but this effect becomes less important for lower-opacity lines (Muzerolle et al. 2001). Similarly, lower- \dot{M} magnetospheres will have lower densities and the absorption may appear even in H α . In some cases, the redshifted absorption occurs over only a small range of rotational phases, which could be explained if accretion occurs in relatively narrow funnels. As shown in **Figure 7** for the case of V2129 Oph, the redshifted absorption appears only when the alignment of the flow along the line of sight is optimal (Alencar et al. 2012), similar to the classic case of the funnel flow of AA Tau (Bouvier et al. 2007).

The width and location of a redshifted absorption feature probe the range of velocities along the line of sight where the feature forms. The He I 10,830-Å line is particularly suitable for this type of analysis because the lower level is metastable, increasing its population and making the line prone to absorption (e.g., **Figure 6**). In addition, the He I 10,830-Å line is the only radiative transition allowed between the lower and upper levels, making it a scattering line (Fischer et al. 2008). Redshifted absorption in this line is an extremely sensitive indicator of accretion, being strong even in the lowest accretors (Edwards et al. 2006, Ingleby et al. 2011). Redshifted absorption components in emission lines of singly and doubly ionized metals have been used to map the structure of the flow, yielding increasing temperature and density with velocity of the maximum absorption depths (Petrov et al. 2014). Infall with velocities $>400 \text{ km} \cdot \text{s}^{-1}$ may also be seen in the BCs of hot FUV lines, such as CIV (e.g., Ardila et al. 2013).

Although the models discussed here represent the current paradigm, it has recently been proposed that the broad components of optical and near-IR lines of hydrogen are instead formed in the turbulent postshock region, based on correlations between postshock indicators and changes in line profiles (Dupree et al. 2014). However, the fluxes of the strong hydrogen lines require emission from spatially extended regions (Calvet et al. 1984); in addition, the lack of any polarization signature in the H α line of TW Hya indicates that it is formed over a large volume with no ordered field (Yang et al. 2007). Similarly, formation of the extended wings in the preshock region is unlikely, given the small size of the region (Equation 10). Moreover, calculated profiles of lines arising in this region are centered around the free-fall velocity, in contrast to the observed breadth of the line (Lamzin 2003). Additional calculations of line fluxes and profiles from models are needed to demonstrate whether the turbulent model is viable.

Overall, the observations are consistent with general predictions of the accretion shock model, although the detailed line profiles depend on flow inhomogeneities and nonaxisymmetric geometries, which require detailed simulations to explain.

2.3.3. Winds and outflows. Strong mass ejection from CTTS in the form of jets and blueshifted forbidden emission lines (e.g., the [OI] line in **Figure 6**) has been recognized for decades [see reviews by Bally (2016) and Frank et al. (2014)]. These strong winds and outflows are clearly

accretion-powered, as they occur only in systems with near-IR excesses (and in many cases with large accretion shock veiling) and with mass loss rates that strongly correlate with accretion luminosity (e.g., Hartigan et al. 1995, Rigliaco et al. 2013, Natta et al. 2014). In the standard picture, the winds and jets are driven by rotating magnetic fields anchored somewhere in the inner disk (see the discussion in Section 3.2), although launching by other mechanisms can be important (Ferreira et al. 2006). In addition to forbidden line emission, the outflows may also lead to blueshifted absorption components superimposed on background (magnetospheric) emission (as in $H\alpha$ in **Figure 6**) or on the stellar accretion shock plus photospheric continuum (as in the He I 10,830-Å lines in **Figure 6**). A full discussion of the different wind and outflow components is beyond the scope of this review; here we focus on what may be learned from prominent P Cygni line profiles.

Calculations of line profiles from magnetically accelerated winds arising from the inner disk have been made, including the emission from either axially symmetric magnetospheres (Lima et al. 2010, Kurosawa et al. 2011) or funnel flows consistent with Romanova et al.'s (2004) infall simulations (Kurosawa & Romanova 2012). These models reproduce the main observed features of the hydrogen lines for accretion rates within observed ranges. In particular, synthetic line profiles produced in the models exhibit blueshifted absorption components in some lines at $\sim 100\text{--}200 \text{ km} \cdot \text{s}^{-1}$ superimposed on the blue wings of the infall emission profiles. The absorption depth increases with accretion rate, wind temperature, and inclination. The wind signatures are usually absent in Paschen lines, even when present in Balmer or He I lines (Edwards et al. 2003, 2006).

The disk wind models used in these calculations have so far been limited in scope. The models usually include outflow only from the inner disk (Kwan et al. 2007, Kurosawa et al. 2011, Kurosawa & Romanova 2012), in part because of the complexity of modeling the inner magnetospheric emission that can be absorbed by the outflow. Because of the geometry, these inner-disk winds generally produce narrow blueshifted absorption; such features can explain $\sim 30\%$ of the observed profiles, but cannot explain the broad absorption seen at higher velocities from many other objects. However, if the disk wind is not limited to a narrow region in the inner disk, but emerges over a substantial range in disk radii (Section 3.2), it is conceivable that broader absorption could extend to lower velocities, as the outflow velocities should scale with the Keplerian velocities at the flow footpoints in the disk.

The He I 10,830-Å line has drawn increasing attention in recent years as a sensitive probe of both infall and outflow (Dupree et al. 2005, Edwards et al. 2006; see also **Figure 6**). Some objects exhibit line profiles characteristic of magnetospheric flows, whereas in other cases, blueshifted wind absorption is strong. The wind features only appear in CTTS, indicating that the outflows are powered by accretion energy (Edwards et al. 2006). However, it has been suggested that the He I profiles with broad (in velocity) absorption components require a more spherical and/or polar outflow than predicted for typical disk wind models (Kwan et al. 2007, Kurosawa et al. 2011, Kurosawa & Romanova 2012). In turn, this could indicate that the mass loss originates from the stellar surface (Edwards et al. 2006, Kwan et al. 2007, Dupree et al. 2014).

The strongest evidence for a stellar wind is provided by TW Hya, one of the closest and best-studied of all CTTS. The He I 10,830-Å profile in this star shows deep (to near-zero residual intensity), broad blueshifted absorption extending to $\sim 200 \text{ km} \cdot \text{s}^{-1}$ (Dupree et al. 2005, 2014; Edwards et al. 2006). As TW Hya is observed nearly pole-on, it is extremely difficult to see how absorption in a disk wind can obscure nearly all of the stellar photosphere (which is the background continuum source) over a wide range of velocities. Detailed modeling has not yet been done to see if the mass loss rate is large enough to require accretional driving, or whether enhanced solar-type activity could be responsible.

Although analyses of jets and forbidden-line outflows indicate temperatures of only $\sim 10^4$ K (Bally 2016), it has been suggested that some of the outflowing gas has high (i.e., nearly coronal) temperatures, which might also suggest a stellar rather than a disk origin. Dupree et al. (2005, 2014) infer the presence of a hot spherical wind from the sharp drop on the blue side of the CIII, OVI, CIV, and NV lines (see **Figure 5**) and similarly postulate the presence of a spherical accelerating wind, with temperatures increasing with distance and a mass loss rate of the order of a few $10^{-11} M_{\odot} \cdot \text{year}^{-1}$. However, Johns-Krull & Herczeg (2007) do not find evidence for absorption in these hotter lines and instead suggest that this wind is cool and photoionized by FUV and X-ray radiation.

Because the blueshifted HeI absorption is only seen in accreting systems, this raises the question of whether the outflow can be excited by the energy released by the magnetospheric infall. Cranmer (2008, 2009) developed models in which time-dependent accretion creates turbulence that is then transmitted via MHD waves to drive the stellar wind. A potentially attractive aspect of such a wind is that it would be magnetically coupled directly to the stellar surface, and thus might help spin down the star (Matt & Pudritz 2005, Matt et al. 2012); but whether this mechanism really can drive sufficiently large outflows is not clear.

2.4. Characteristics of Accretion in Pre-Main-Sequence Stars

2.4.1. Methods for measuring the accretion rate. Calculating a mass accretion rate requires estimates for the accretion luminosity and the stellar mass and radius (Equation 3). Accretion luminosities were first measured directly from excess Balmer continuum emission and the Balmer jump in blue spectra (e.g., Bertout et al. 1988; Basri & Bertout 1989; Valenti et al. 1993; Gullbring et al. 1998, 2000) and from the veiling of photospheric emission (Basri & Batalha 1990; Hartigan et al. 1991, 1995). The results from these surveys have since been adapted to broadband imaging surveys that include U-band (or u-band) photometry (e.g., Hartmann et al. 1998, White & Ghez 2001, Robberto et al. 2004, Sicilia-Aguilar et al. 2010, Rigliaco et al. 2011). In these methods, the accretion continuum is measured over some wavelength range. A bolometric correction is then applied to convert the measured continuum emission to a total accretion luminosity. The bolometric correction may be obtained from shock models (Calvet & Gullbring 1998, Ingleby et al. 2013; see also Section 2.3), from simple plane-parallel hydrogen slab models (e.g., Bertout et al. 1988, Basri & Bertout 1989, Valenti et al. 1993), or by assuming $\sim 10^4$ -K blackbody emission (e.g., Mendigutia et al. 2011). The slab models were developed to describe the boundary layer interpretations for CTTS and are still in use today as an empirical description of the excess continuum emission (e.g., Valenti et al. 1993, Herczeg & Hillenbrand 2008, Manara et al. 2014). Direct measurements of accretion rates have been made for intermediate-mass and HAeBe stars (Calvet et al. 2004, Donehew & Brittain 2011, Mendigutia et al. 2011, Fairlamb et al. 2015) down to the substellar regime (e.g., Herczeg et al. 2009, Rigliaco et al. 2012, Zhou et al. 2014).

For some stars, such as those that are heavily extincted (for example, protostars embedded in envelopes; see Section 4.3), the excess continuum emission is difficult or impossible to measure. This limitation motivated the use of emission lines as secondary accretion rate measurements, where a line luminosity or shape is converted to an accretion luminosity on the basis of correlations from stars where both are measured (e.g., Muzerolle et al. 1998, Natta et al. 2004, Mohanty et al. 2005, Dahm 2008, Herczeg & Hillenbrand 2008). Use of near-IR lines in particular minimizes the effect of uncertainties in extinction corrections (e.g., Muzerolle et al. 1998, Calvet 2004, Natta et al. 2006, Salyk et al. 2013, Rigliaco et al. 2015); mitigates confusion with Balmer line absorption in the photospheres of HAeBe stars (e.g., García-López et al. 2006, Salyk et al. 2013); and makes possible detections for very faint planetary-mass objects (Joergens et al. 2013), especially when

high-contrast observations with adaptive optics are necessary (Bowler et al. 2011). Emission-line correlations with accretion rates have also been applied to large samples of multiobject spectra to survey accretion in regions of different ages or metallicities (e.g., Fang et al. 2009, Kalari & Vink 2015).

When measured simultaneously, correlations between line and continuum emission have a scatter of 0.25–0.4 dex (Alcala et al. 2014). This scatter probably arises from real differences in accretion flow properties, including the presence of multiple components of different temperatures and densities, differences in the geometry of the flow, and differences in the inclination at which we view the flow. Emission from winds in particular may contaminate the emission from accretion in Herbig Be (HBe) (e.g., Kraus et al. 2008) stars and perhaps young protostars. The H α emission line full width at 10% maximum is a useful diagnostic of the presence of accretion but does not provide an accurate estimate of the accretion rate (e.g., Antonucci et al. 2011, Fang et al. 2013, Alcala et al. 2014). Modeling the H α line profile (see Muzerolle et al. 2005 and the references therein) provides results that are internally self-consistent but may have systematic differences with accretion rates calculated from direct measurements of the accretion continuum, in large part because of the ad hoc nature of the assumed temperature distribution in the magnetosphere.

Thus, direct measurements of accretion rates are typically uncertain by a factor of a few, with random uncertainties that are dominated by systematic and methodological challenges in calculating stellar parameters, especially stellar mass and extinction (see discussions in Herczeg & Hillenbrand 2008; Manara et al. 2013b, 2015). Recent improvements in accretion rates have been driven by the use of broadband, flux-calibrated optical spectra from instruments such as VLT/X-Shooter to measure simultaneously the accretion continuum flux, the photospheric temperature and flux, the extinction, and many emission lines (Rigliaco et al. 2012; Ingleby et al. 2013; Alcala et al. 2014; Manara et al. 2014, 2015). These broadband analyses of accretion and photospheric properties have significantly reduced observational uncertainties; spectral analysis with a single methodology has improved the precision and reduced scatter in estimates of accretion rate. Dedicated multiobject spectroscopic campaigns are also producing consistent stellar parameters on large samples (Cottaar et al. 2014, Frasca et al. 2015) and should significantly reduce random errors in stellar parameters. Other uncertainties are substantial but smaller. Bolometric corrections differ by ~ 0.3 dex, depending on the parameters used to describe the emission region. The veiling at red-optical wavelengths is typically larger than expected from models (e.g., Fischer et al. 2011, McClure et al. 2013) and is usually excluded in luminosity measurements, with rare exceptions (Ingleby et al. 2013). For strong accretors, line emission may help to fill in the photosphere and may lead to overestimates of the accretion continuum flux when measured from veiling (Gahm et al. 2008, Petrov et al. 2011, Dodin & Lamzin 2012). Many of the uncertainties in direct accretion rates are hard-wired into the absolute uncertainty in secondary accretion rate measurements, although the use of near-IR lines minimizes extinction-related errors. For each accretion diagnostic, mass-dependent sensitivity limits (e.g., White & Basri 2003, Ingleby et al. 2011, Manara et al. 2013a) and selection biases affect how accretion rates vary with stellar and disk properties.

2.4.2. Accretion rate versus stellar mass. The accretion rate is found to correlate with the stellar mass, $\log \dot{M} \propto M_{*}^{\alpha}$, where α ranges from 1.5 to 3.1 (e.g., Muzerolle et al. 2003, Calvet 2004, Herczeg & Hillenbrand 2008, Fang et al. 2009, Alcala et al. 2014, Antonucci et al. 2014, Manara et al. 2015). The best fit from our selected compilation of accretion rates measured from spectroscopic measurements of the Balmer continuum is

$$\log \dot{M} / (M_{\odot} \cdot \text{year}^{-1}) = -7.9 + 2.1 \times \log M_{*}, \quad (11)$$

as measured for accreting stars between 0.1 and $1.0 M_{\odot}$ and excluding upper limits of nonaccreting stars and severe outliers in age (see **Figure 8**). Half of the difference between $\alpha = 2.1$ calculated here and 1.8 from the Lupus sample of Alcalá et al. (2014) is attributed to different masses estimated from stellar evolutionary models, with the remaining difference attributed to sample selection. The HAeBe sample of Fairlamb et al. (2015) shows a steeper slope, which may be partially introduced by the large number of upper limits on accretion rates for stars that are thought to still be actively accreting. The accretion rates measured from emission lines yield a similar relationship, with $\alpha = 2.4$ – 2.7 depending on the selected mass range. However, accretion rates measured photometrically from excess U-band emission are nearly flat with mass.

The scatter in this fit is ~ 0.75 dex, with a total range in accretion rate of about two orders of magnitude at any given stellar mass. The slope decreases to ~ 1.9 if the fitted mass range extends to $2 M_{\odot}$, although the exclusion of upper limits is a more serious bias for hotter stars. The survey by Alcalá et al. (2014) of accretion in a subset of Lupus stars has a scatter of 0.4 dex, which may be smaller either because of selection biases or because the cluster is older than Taurus and is missing strongly accreting members. Much of this scatter is real, as the full range in accretion rates is too large to be attributed entirely to the ~ 0.5 dex that can be explained by variability (e.g., Venuti et al. 2014; see also see Section 2.5).

2.4.3. Accretion rate versus stellar age. Models of disk evolution through viscous accretion predict a decline in accretion rate with age (Hartmann et al. 1998, Alexander & Armitage 2009, Gorti & Hollenbach 2009). The empirical relationship between accretion rate and age is uncertain. Some surveys within clusters indicate that accretion rates decrease as t^{α} , where α ranges from -1.6 to -1.2 (Hartmann et al. 1998, Sicilia-Aguilar et al. 2010, Manara et al. 2012, Antonucci et al. 2014, Venuti et al. 2014). Our compilation from the spectroscopic Balmer excess measurements and excess line emission yields

$$\log \dot{M} / (M_{\odot} \cdot \text{year}^{-1}) = -1.32 - 1.07 \log t \text{ year}^{-1}, \quad \text{for } M_{*} = 0.7 M_{\odot}, \quad (12)$$

with a scatter of 0.5 dex. However, these results are complicated by the challenges posed in measuring the age of any specific young star (see the review by Soderblom et al. 2014) and by the difficulty in evaluating the dependences on both mass and age simultaneously. The uncertainties in accretion rate are correlated with the uncertainties in age, which could lead to a spurious relationship. However, for their analysis of the Orion Nebula Cluster, Da Rio et al. (2014) suggest instead that the relationship between age and accretion rate may be steeper than measured because of the different observational biases in their sample.

Some studies circumvent the uncertainties in individual stellar ages by comparing accretion rates between stellar groups, dispersed populations, and/or clusters with assumed common ages. There is a possible deficiency of very strong accretors at old ages (Calvet et al. 2005), although some still persist (Ingleby et al. 2014). Manara et al. (2015) found that accretion rates in the ~ 1 -Myr-old Ophiucus star-forming region are similar to those in the ~ 3 -Myr-old Lupus star-forming region, much less than the ~ 0.5 -dex decrease expected for the viscous disk evolution described by Hartmann et al. (1998). In an alternative approach, Venuti et al. (2014) and Kalari et al. (2015) found that strong accretors are more spatially concentrated and therefore younger than weak accretors in the Lagoon Nebula and NGC 2264. Further comparisons are needed to increase sample sizes and to account for selection effects and methodological differences.

The decay of accretion cannot be modeled entirely as a power law with time; instead, there must be a phase of rapid decay to explain the decline in the fraction of accreting stars with age. The timescale to evolve from a significantly accreting, optically-thick disk is short, as assessed from near- and mid-IR emission from warm disk dust (e.g., Haisch et al. 2001, Hernández et al.

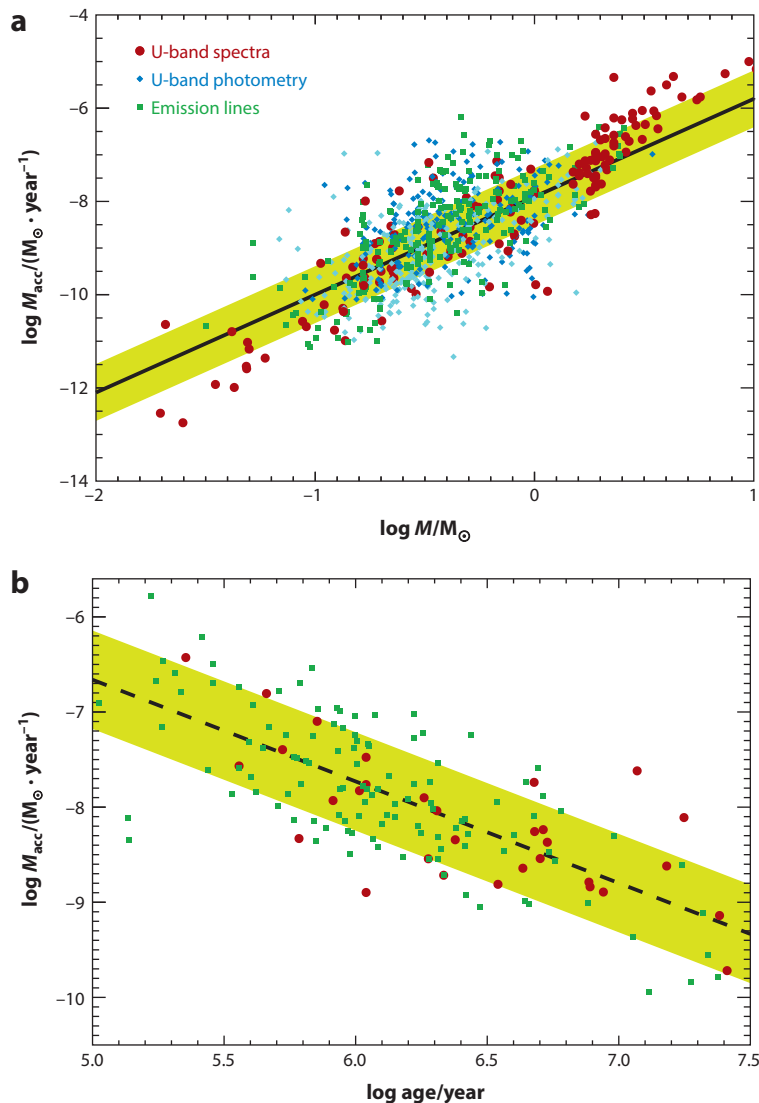


Figure 8

(a) Accretion rate versus stellar mass and (b) age for accretion rates obtained from spectroscopic measurements of the Balmer continuum (*red circles* from Calvet 2004, Herczeg & Hillenbrand 2008, Herczeg et al. 2009, Rigliaco et al. 2012, Ingleby et al. 2013, Alcalá et al. 2014, Fairlamb et al. 2015); from photometric U-band measurements (*blue diamonds* from Sicilia-Aguilar et al. 2010, Rigliaco et al. 2011, Venuti et al. 2014; *cyan diamonds* from the Orion Nebula Cluster sample of Manara et al. 2012; *diamonds* not shown in panel b); and from emission lines (*green squares* from Fang et al. 2009, Antonucci et al. 2014, Manara et al. 2015). For all samples, masses and ages are calculated from pre-main-sequence models of Baraffe et al. (2015) and nonmagnetic tracks of Feiden (2016), with the updated masses applied to the accretion rates. The data shown on the mass–accretion rate plot (a) are restricted to stars with age estimates between 0.1 and 30 Myr. The lines and shaded regions show the best linear fits and $1 - \sigma$ scatter. The mass–accretion rate relationship is calculated for objects with mass between 0.05 and $1 M_{\odot}$. The accretion rates in panel b are shown only for 0.3– $1.0 M_{\odot}$ and are scaled by the $M - \dot{M}$ relationship (a) to $0.7 M_{\odot}$. The relationship between age and accretion rate may be strongly biased by correlated observational uncertainties between accretion rates and age estimates.

2007), gas (e.g., Pascucci et al. 2006, Ingleby et al. 2009), or accretion rates (Fedele et al. 2010). Simple viscous accretion is unlikely to explain these rapid turn-offs of accretion (Clarke et al. 2001). Instead, either photoevaporation (e.g., Gorti & Hollenbach 2009, Owen et al. 2012) or gap opening by planets is more plausible. A thorough assessment of disk dissipation can be found in the review by Alexander et al. (2014).

2.4.4. Accretion from disks with inner cavities. The accretion rate is likely sensitive to the complexity of circumstellar disk structures. However, correlations between accretion and disk structure have only been evaluated for transition disks, which have inner cavities in their dust distributions that may be related to planet formation or disk dispersal (see the review by Espaillat et al. 2014). Accretion probes the content of the inner 1 AU of the disk, which complements gas diagnostics at other wavelengths. Comparing accretion rates of transitional disks to those of full disks indirectly informs how much gas is left in the inner cavity and may thereby discriminate between different physical mechanisms that can carve out inner holes (e.g., Najita et al. 2007, Zhu et al. 2011).

Accretion is ongoing in ~ 70 – 80% of stars with transitional disks (e.g., Kim et al. 2009, Cieza et al. 2010, Merin et al. 2010). For the set of transitional disks with ongoing accretion, it remains unclear whether that accretion is weaker than expected for the stellar mass. Manara et al. (2014) found that many transitional disks accrete at rates similar to full disks. The methodology to calculate accretion rates was systematically consistent in both the transitional disk and control samples, but the two samples came from different regions with a range of ages. However, Najita et al. (2015) found that transitional disks in Taurus and Ophiucus have low accretion rates relative to their stellar mass and especially their disk mass. In this case the ages of the transition disks and of the control samples are thought to be similar, but the accretion rates were compiled from sources that used different methods for calculating accretion rates. Completeness of the control samples may also skew the results. Recent high-resolution Atacama Large Millimeter Array (ALMA) studies have suggested that the gas interior to the dusty region is depleted (van der Marel et al. 2015) by at least an order of magnitude, and in some cases by factors of more than 10^2 – 10^4 (van der Marel et al. 2016); however, such extremely large depletions may be difficult to reconcile with even modest decreases in gas accretion rates. In any event, it seems clear that the depletion of small dust in the inner cavity is generally much greater than the gas depletion, posing challenges to theories (e.g., Zhu et al. 2011).

2.5. Variable Accretion Flows

Variability is one of the defining characteristics of T Tauri stars (Joy et al. 1945). Photometric campaigns with sporadic cadence clearly demonstrate that accretion variability, extinction events, and stellar spots all contribute to the rich variability of T Tauri stars (e.g., Herbst et al. 1994, Grankin et al. 2007). In this section we concentrate only on changes in accretion. Recent dedicated photometric campaigns, including a month-long campaign to continuously monitor NGC 2264 with COROT (the *Convection Rotation and Planetary Transits* satellite) and the *Spitzer Space Telescope* (*Spitzer*) (Alencar et al. 2010, Stauffer et al. 2014), have successfully discriminated between different sources of variability (see **Figure 9**). Meanwhile, systematic optical wide-field sky surveys for transients are supplanting the substantial prior contributions from amateur astronomers (e.g., Jones 2008), and have discovered FU Ori and EX Lup-type outbursts (see below) at a rate of a ~ 1 per year, leading to estimates for an FUor outburst rate of $\sim 10^{-4}$ per accreting star per year (e.g., Hillenbrand & Findeisen 2015). These strong outbursts may be especially important during the main growth phase of a star (Section 4), but the optical focus of transient surveys at optical wavelengths means that only a few outbursts have been identified in heavily embedded protostars (e.g., Kóspál et al. 2007, Safron et al. 2015).

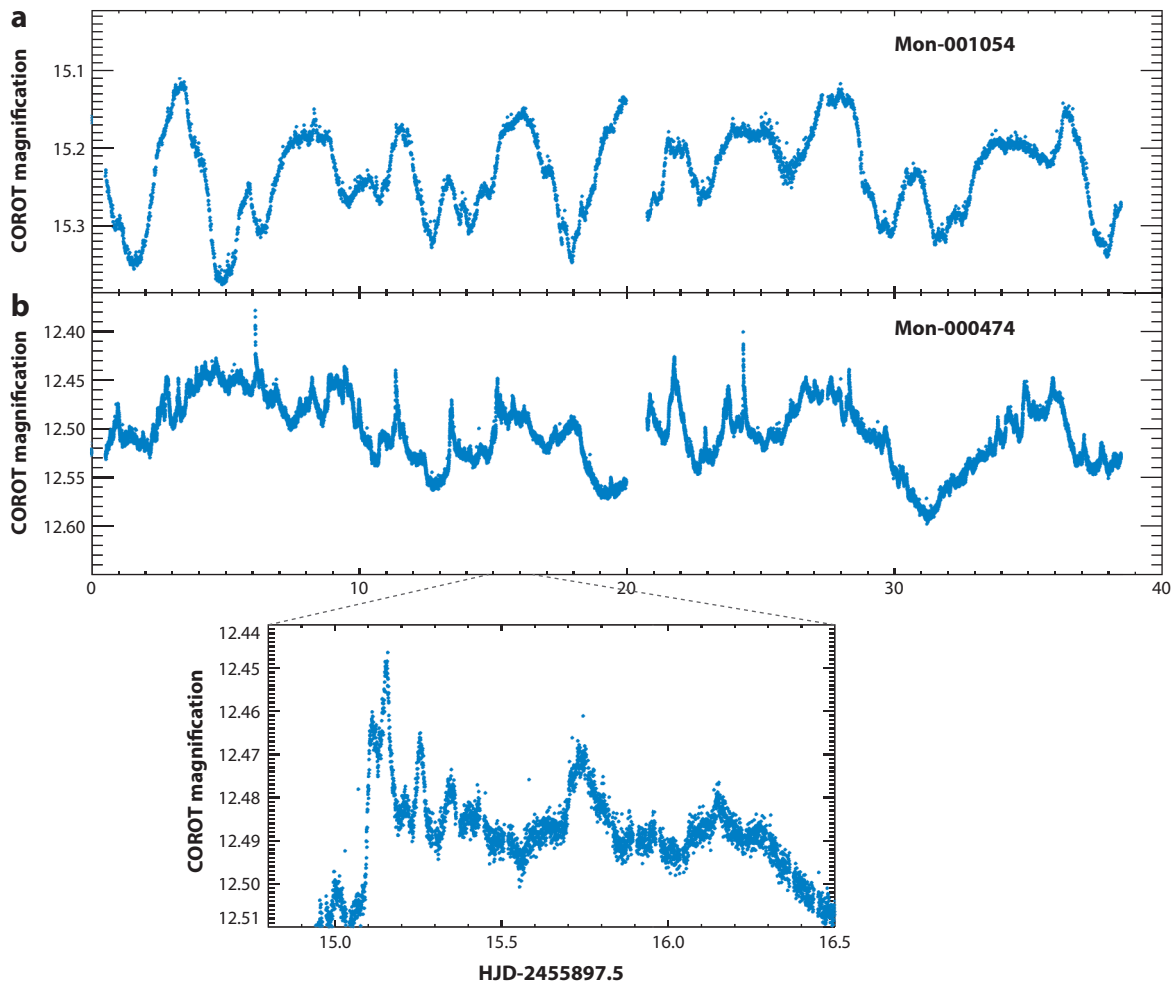


Figure 9

COROT lightcurves of two objects in NGC 2264 (Cody et al. 2014, Stauffer et al. 2014) showing (a) irregular accretion variability and (b, with *inset*) irregular accretion with short bursts. Units are in days. Courtesy of Ann Marie Cody.

The shortest timescales for changes in mass inflow are expected to be flow timescales: For typical parameters, $R_{\text{co}}/(0.5v_{\text{ff}}) \approx$ a few hours. Winding up of magnetic field lines connecting a star with non-corotating regions of its disk might result in variations owing to reconnection on a few rotation periods. Magnetospheric structures may rotate into and out of our view, making intrinsic variations difficult to study on week-long (rotational) timescales. Finally, longer-term variations could be caused by structures in the disk varying the mass transport on viscous timescales R^2/ν , which can be weeks, months, years, or longer, depending upon the radius at which the variability is triggered and the level of viscosity ν (if any; see Section 3). These variations are likely seen in months-long EXor outbursts and decades-long FUor outbursts. EXor and FUor outbursts are often grouped together because of similar detection methods and because these two possibilities are sometimes challenging to distinguish from each other. However, FUor outbursts

are events that are 10–1,000 times larger in mass than EXor outbursts, are likely caused by distinct physics, and are described separately below.

2.5.1. Short-timescale changes in the accretion flow. Unstable magnetosphere–disk interactions are thought to control accretion modulations on short timescales. Although accretion flow appears to be stable for some stars, other stars have irregular lightcurves that indicate rapid changes in accretion. Romanova et al. (2008) used 3D MHD simulations of accretion to develop a framework to interpret these differences as stable and unstable regimes for the magnetic Rayleigh–Taylor instability at the magnetosphere–disk interaction region. In the stable regime, which is associated with large truncation radii relative to the corotation radius (low accretion rates or strong dipole fields), the accretion flow occurs in two funnel flows that may periodically intercept our line of sight and cause inverse P Cygni absorption similar to that of AA Tau–like stars. In the unstable regime (small magnetospheric radius owing to strong accretion or weak dipole fields), the redshifted absorption is persistent but has a depth that varies on timescales of ~ 1 day (Kurosawa & Romanova 2013). Blinova et al. (2016) further split the unstable regime into an ordered unstable regime, which occurs when the disk truncation radius is much smaller than the corotation radius, and a chaotic unstable regime, which occurs when the disk truncation radius is similar to the corotation radius. The ordered unstable regime results in 1–2 accretion streams, whereas in the chaotic unstable regime several distinct streams may be present at any time and may randomly form and disappear.

Evidence for these different regimes may be found in dedicated photometric and spectroscopic monitoring programs. In optical photometric monitoring campaigns of NGC 2264 with COROT, most strong accretors showed irregular variability and only four accretors exhibited rotational modulation (Stauffer et al. 2014). Most accretors had short accretion bursts with an occurrence rate of 0.2 day^{-1} in addition to longer-timescale variations. These bursts last for durations as short as 4 h and are typically 0.05–0.3 mag in strength, although the increase in accretion is larger when corrected for the contribution from the stellar photosphere. A 3–4-h timescale for bursts has also been seen in X-rays (Kastner et al. 2002, Brickhouse et al. 2010) and is similar to the timescale for gas from the truncation radius to fall onto the star, although a ~ 2 -h delay between the X-rays and the photospheric heating may be present (Dupree et al. 2012). These types of changes are similar to those seen in smaller monitoring campaigns with high cadence over several rotational periods (Rucinski et al. 2008, Siwak et al. 2011), and have also been seen on very low-mass stars and brown dwarfs (Grosso et al. 2007a, Cody & Hillenbrand 2014).

The COROT and related *Spitzer* monitoring campaigns have provided high-time-resolution photometry, but conversions of photometric variations to accretion rates are only inferred with some uncertainty owing to the underlying photospheric flux. To complement this effort, Venuti et al. (2014, 2015) monitored NGC 2264 in the U-band, which produces more reliable accretion rates because of greater contrast with the stellar photospheric fluxes (**Figure 2b**), and found that accretion rates vary by ~ 0.06 dex on hours-long timescales and by ~ 0.5 dex on weeks-long timescales. They attributed the majority of the changes on weeks-long timescales to rotational modulation of the accretion flow. This level of variability is consistent with that inferred from spectroscopic surveys from veiling of individual objects (e.g., Alencar & Batalha 2002, Donati et al. 2011) and from emission line variability in repeated observations of many objects (e.g., Nguyen et al. 2009, Costigan et al. 2012, Fang et al. 2013). Inferring accretion variability from changes in emission line fluxes requires the use of global correlations between accretion rate and line luminosity, which may not apply to variability of a single source. In rare cases, a star may appear to be actively accreting in one epoch and not accreting in a different epoch (Bayo et al. 2012, Fang et al. 2013). Direct monitoring of the NUV continuum shock emission indicates variability on

timescales of months, consistent with changes in the density of accretion columns (Ingleby et al. 2015); these changes seem to be linked to changes in the density of the inner disk, although more extensive monitoring is required to interpret the nature of this link.

In contrast to the irregular variability seen in accretion rate indicators, magnetospheric structures endure over many rotation periods. In AA Tau and other stars with periodic extinction events, accretion funnels consistently pass through our line of sight with only modest orbit-to-orbit changes (Bouvier et al. 2007, Cody et al. 2014). However, when comparing COROT lightcurves of NGC 2264 obtained 3 years apart, Sousa et al. (2016) found that some periodic dust obscurations became aperiodic and vice versa, suggesting that switching from stable to unstable regimes is common. Similarly, Zeeman–Doppler imaging campaigns have shown that the magnetic morphology and the resulting accretion structures are relatively stable on weeks-long timescales (e.g., Donati et al. 2011, Alencar et al. 2012), but the field strengths and polarity may change from year to year (Donati et al. 2012). The contrast between this inferred stability and the irregularity of accretion rate estimates may be related to sample selection. Stars with irregular lightcurves and strong bursts tend to be strong accretors relative to their mass, whereas those with deep, sharp drops in light interpreted as disk warps blocking our line of sight to the star tend to be weaker accretors (Stauffer et al. 2014). The Zeeman–Doppler imaging sample may also be biased to weak or moderate accretion rates. Within the context of the accretion models of Romanova et al. (2008) and Blinova et al. (2016), weak accretion may relate to stable magnetic morphologies, whereas strong accretion may be related to chaotic instability. Alternatively, the different methods may be revealing different phenomena, where the magnetic morphology of accretion is stable but the mass loading on magnetic field lines has irregular variability and bursts.

If stellar magnetic field lines cannot slip through the inner-disk gas sufficiently freely, the field lines may wind up and bulge outward (Lovelace et al. 1995, figure 1). Material in this bulge can be ejected as the field reconnects in a pre-main-sequence version of a coronal mass ejection (Hayashi et al. 1996, Goodson et al. 1997, Zanni & Ferreira 2013). This may explain some of the variability seen in T Tauri flows and could be important in regulating stellar angular momentum (Zanni & Ferreira 2013). Reconnection events as the star–disk magnetic fields wind up may also result in bright flares in hard X-rays on long (0.1-AU) magnetic structures (Favata et al. 2005).

2.5.2. EXor outbursts. EXor outbursts are defined by (and misnamed after) the prototype EX Lup, which has had several 6-month outbursts of ~ 5 mag over the past hundred years of monitoring (e.g., McLaughlin 1946, Herbig 1977, Kóspál et al. 2008). About 15 EXor objects or candidates have been identified, although this classification is only loosely defined and may capture a range of behaviors (e.g., Herbig 1989, Lorenzetti et al. 2012). For example, the binary CTTS VY Tau is classified as an EXor based on a series of outbursts and fades over 20 yr, starting in the 1950s, after which it returned to a quiescent state (Herbig 1990). In general, an EXor eruption is interpreted as a 10–100-fold increase in accretion rate that lasts from months to a few years (e.g., Aspin et al. 2010, Lorenzetti et al. 2012, Sicilia-Aguilar et al. 2012). The brightness increase may be much larger if the accretion burst is accompanied by a large change in extinction, as is the case for V2492 Cyg (Hillenbrand et al. 2013). Ongoing transient searches identify about one new EXor outburst per year (e.g., Covey et al. 2011, Holoien et al. 2014, Kun et al. 2014), with classification based on outburst duration and size.

In quiescence, EXors have similar spectra, spectral energy distributions, and accretion rates to those of CTTS (e.g., Herbig 2008, Kóspál et al. 2011). Their magnetospheric accretion structures are stable, and their emission lines have distinct broad and narrow components (Sicilia-Aguilar et al. 2015). In outburst, their accretion rates increase to $\sim 10^{-7} M_{\odot} \cdot \text{year}^{-1}$, their optical and near-IR emission lines become bright, and their optical photosphere is strongly veiled by an accretion

continuum (e.g., Aspin et al. 2010, Kóspál et al. 2011, Sicilia-Aguilar et al. 2012). Disk heating during the 2008 outburst of EX Lup has been associated with the formation of crystalline silicates and with emission in warm H₂O and OH lines (Ábrahám et al. 2009, Banzatti et al. 2012, Juhász et al. 2012).

The timescales on which EXor outbursts occur and persist suggest that they are related to instabilities in the inner disk. Material builds up in the inner disk when more gas is accreted into the inner disk than is accreted from the disk onto the star. Banzatti et al. (2015) found support for this gas buildup in a factor-of-10 drop in the CO surface density in the inner disk between outburst and quiescence.

A possible physical framework for this scenario, developed by D'Angelo & Spruit (2010, 2012), is magnetospheric instabilities in the star–disk interaction region. In the quiescent state, the stellar magnetosphere truncates the disk beyond the corotation radius, which inhibits accretion. As the gas surface density and gas pressure increase, the truncation radius pushes inward until the truncation radius is smaller than the corotation radius, allowing the gas at the inner disk to accrete onto the star. The gas pressure then decreases, so the magnetospheric radius expands beyond the corotation radius to again halt accretion until another eruption. A challenge for this scenario is to explain the substantial accretion rates detected during quiescence, when the large truncation radius is supposed to inhibit accretion. In an alternate scenario, Zhang et al. (2015) speculate that EXor outbursts may result from small instabilities within the disk. They find CO gas infalling at 6 km · s⁻¹ during a deep extinction event of AA Tau (Bouvier et al. 2013) and suggest that this infalling gas may be a predecessor to a future EXor outburst.

2.5.3. FU Ori outbursts. A small set of pre-main-sequence stars, the FU Ori objects, show optical outbursts of several magnitudes or more, with decay timescales of decades to centuries (Figure 10). As discussed in the review by Hartmann & Kenyon (1996) (for a recent update, see Audard et al. 2014), the outbursts are the result of the onset of rapid disk accretion at rates of

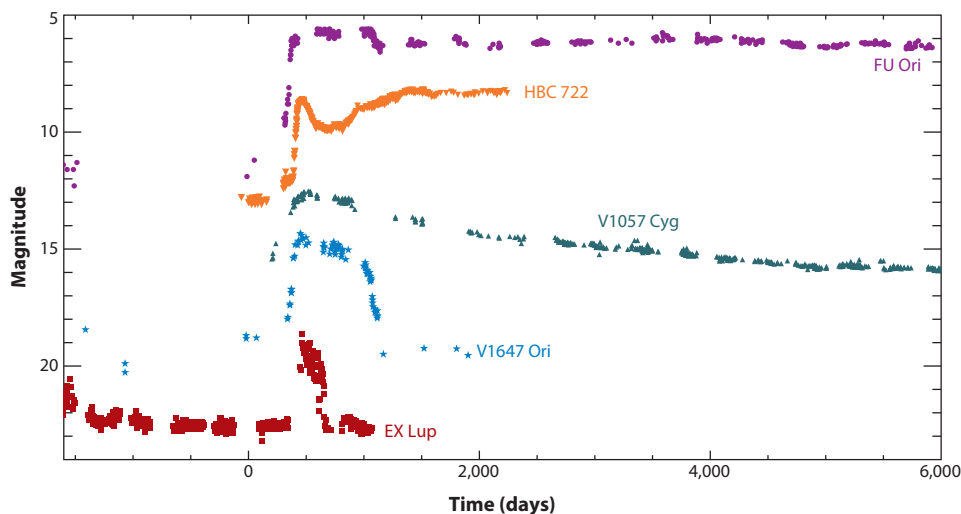


Figure 10

Lightcurves of FUor outbursts of FU Ori and HBC 722; EXor outbursts of EX Lup and V1647 Ori; and an intermediate outburst of V1057 Cyg. Adapted from Kóspál et al. (2011) with permission.

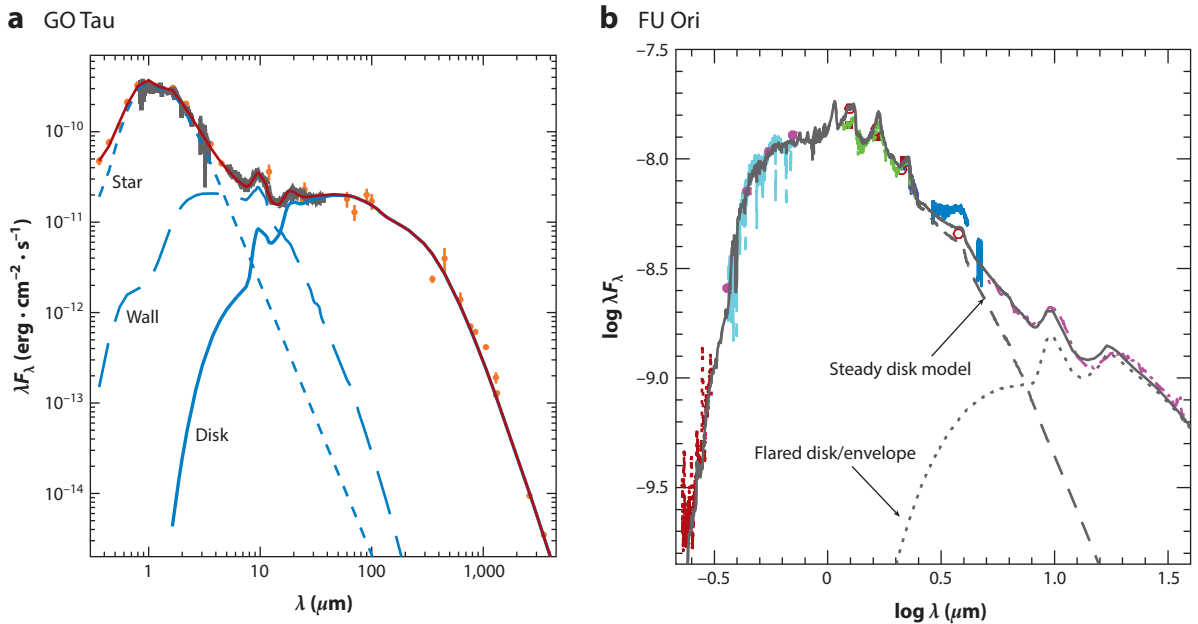


Figure 11

(a) Spectral energy distribution (SED) of the classical T Tauri star GO Tau. The blue/near-ultraviolet excess over the stellar photosphere indicates the presence of accretion, and the excess emission at long wavelengths is produced by stellar and accretion shock irradiation of the disk and its inner wall. The silicate emission features at 10 μm and 18 μm indicate a vertical temperature inversion, as expected from external heating of the disk. (b) Steady accretion disk model SED for FU Ori compared with observations. In contrast to the T Tauri disk, the absorption lines and molecular bands of the FU Ori disk show that it is internally heated out to radii of order 1 AU. Radiation from the inner disk heats the upper disk layers at larger radii, producing the silicate emission features. Proceeding from short to long wavelengths, data from the *Hubble Space Telescope*, ground-based spectroscopy and photometry, SpeX, and the IRS spectrometer on the *Spitzer Space Telescope* are shown. Adapted from McClure et al. (2013), Zhu et al. (2007), and Zhu et al. (2009a) with permission. Courtesy of Melissa McClure and Zhaohuan Zhu.

$\sim 10^{-5} - 10^{-4} M_{\odot} \cdot \text{year}^{-1}$. The extended reflection nebulae and/or large extinction of these sources suggest that they represent a (perhaps late) protostellar phase.

The FU Ori objects do not show the signatures of magnetospheric accretion discussed previously, although the few pre-outburst spectra available are consistent with magnetospheric accretion (e.g., Miller et al. 2011). Instead, their accretion luminosities can be inferred from the emission from their self-luminous disks (**Figure 11**), or, for systems that are embedded in a dense dusty envelope, from far-IR luminosities. This is unlike the situation with T Tauri stars whose disks are mostly heated by radiation from the central star and accretion shock.

The most detailed studies have been made of FU Ori itself (**Figure 11b**). Highly detailed modeling of its spectral energy distribution (Zhu et al. 2007, Hartmann et al. 2011), coupled with measurements of rotation out to 4.6 μm (Zhu et al. 2009a), indicate that high surface (effective) temperatures of $\gtrsim 1,000$ K extend out to nearly ~ 1 AU. This result suggests that the magnetorotational instability (MRI) is thermally activated over this region, consistent with the absorption features expected for disks internally heated by viscous dissipation. The decay timescale for the outburst, coupled with the estimate of the active region, leads to an estimate of $\alpha \approx 0.1$, consistent with numerical simulations of the MRI (Zhu et al. 2007). FU Ori also has a strong wind with a

mass loss rate $\sim 10^{-1}$ of the mass accretion rate (Calvet 2004), consistent with the outflow carrying off of order half the accretion energy.

The absence of magnetospheric accretion features is generally understood as a result of the high ram pressures of the disk crushing the magnetosphere against the star. However, the steady-disk spectral energy distribution (SED) models described above indicate that the inner radius of the disk is a factor of two or more larger than that expected for a typical T Tauri star. One possibility is that, at accretion rates approaching $10^{-4} M_{\odot} \cdot \text{year}^{-1}$, the inner disk becomes extremely hot at the midplane, $T \gtrsim 10^5$ K; the geometrically thick disk may then not be able to radiate away much of this thermal energy, instead advecting it into the star (see Hartmann et al. 2011 and references therein). Calculations of the effect of such hot accretion indicate that expansion of the upper layers of the star by the necessary factor is possible (Baraffe et al. 2012), with implications for protostar formation via rapid disk accretion (Section 4.2).

2.6. Accretion in Intermediate-Mass Stars

Intermediate-mass pre-main-sequence stars of masses $\sim 2\text{--}5 M_{\odot}$, evolving on radiative contraction tracks toward the main sequence (corresponding to spectral types FG and early K), exhibit the same signatures of magnetospheric accretion as the lower-mass stars (Calvet 2004); they are also considered to be in the T Tauri class. At later stages, when stars in the mass range $2\text{--}5 M_{\odot}$ near the main sequence, the emission line objects are called H Ae Be stars. These stars bear many of the hallmarks of accretion, including strong emission lines (e.g., Muzerolle et al. 2004, Oudmaijer et al. 2011), excess Balmer continuum emission (e.g., Donehew & Brittain 2011, Mendigutia et al. 2011, Fairlamb et al. 2015), variability in accretion diagnostics (Mendigutia et al. 2013, Costigan et al. 2014), Keplerian disks that extend to near the corotation radius (Vink et al. 2002, Acke et al. 2005, Ilee et al. 2014), and accretion-driven jets (e.g., Grady et al. 2004, Ellerbroek et al. 2014).

Some H Ae Be stars exhibit line profiles characteristic of magnetospheric accretion, including redshifted absorption (Muzerolle et al. 2004) and excess X-ray absorption (Grady et al. 2010). However, it is unclear whether the magnetospheric paradigm applies to most systems. A sharp drop in magnetic activity occurs as a $2\text{--}5\text{-}M_{\odot}$ star evolves across the fully convective–radiative core boundary (Hussain et al. 2009, Gregory et al. 2012), and dynamo-driven magnetic fields seem to disappear. In X-rays, H Ae Be stars are faint and often undetected, indicating a lack of magnetic coronal activity (Stelzer et al. 2006). About 10% of H Ae Be stars possess detected surface-averaged magnetic fields with strengths of ~ 200 G and are among the slowest rotators in the class, whereas the remaining 90% mostly have upper limits of ~ 100 G (Wade et al. 2007, Alecian et al. 2013, Hubrig et al. 2013, Bagnulo et al. 2015) and are generally more rapid rotators. The similarity of the detection fraction and the slow rotation have led to the suspicion that the stars with detected fields are precursors to the magnetic Ap stars (Wade et al. 2007, Alecian et al. 2013). Applying these magnetic field detections or limits, with the relevant accretion rates, to Equation 1 leads to disk truncation radii that are comparable to or even smaller than the stellar radii. For some H Ae Be stars, the disk could reach the stellar surface and accrete through a boundary layer.

Optical and He I 10,830-Å line profiles show some P Cygni and inverse P Cygni profiles, but with some differences when compared to profiles of CTTS (Cauley & Johns-Krull 2014, 2015). Inverse P Cygni profiles are seen only in H Ae stars, with maximum velocities that suggest small disk truncation radii. The lack of redshifted absorption in H Be stars suggests that magnetospheric accretion is not present in these more massive systems. P Cygni profiles are detected from both H Ae and H Be stars, but never from a H Ae star that has redshifted absorption. The He I line profiles of H Ae Be stars also do not show any signatures of a disk wind, which are commonly seen in CTTS spectra. Analysis of line profiles may be complicated by line formation in strong winds. Near-IR

interferometry has shown that Br γ line emission is compact and consistent with magnetospheric accretion for many H Ae stars, but requires extended, presumably wind, configurations for some H Be stars (e.g., Kraus et al. 2008, Eisner et al. 2010).

These properties suggest that H Ae stars have disks with small truncation radii and equatorial magnetospheric accretion flows; the case for magnetospheric accretion is especially tenuous for H Be stars. Further observational studies and simulations of accretion for weak magnetic fields, along with calculations of disk and other winds, are needed to better understand the accretion and ejection of matter in H AeBe stars.

3. THEORIES OF ANGULAR MOMENTUM AND MASS TRANSPORT

Accretion by solar-mass pre-main-sequence stars at rates of $\sim 10^{-8} M_{\odot} \cdot \text{year}^{-1}$ for typical lifetimes of $\sim 1\text{--}2$ Myr imply disk mass reservoirs $\gtrsim 10^{-2} M_{\odot}$, comparable to total disk masses inferred from millimeter-wave dust emission (see Williams & Cieza 2011). Most disk models assume that this mass is distributed over tens if not hundreds of AU (although FU Ori outbursts may require more compact concentrations of mass in the inner disk in some very young systems; see Zhu et al. 2007). The general similarity of disk and inferred accreted masses indicates that some means of mass and angular momentum transport is needed that operates over large radial scales.

It is well established that the MRI can generate turbulence and thus provide the anomalous viscosity needed for efficient accretion in conducting disks (e.g., Balbus & Hawley 1998). However, only the innermost regions ($\sim 0.1\text{--}0.3$ AU) of disks around low-mass stars are likely to have sufficient thermal ionization resulting from stellar and accretion shock heating, perhaps augmented by viscous dissipation (D'Alessio et al. 1999), to sustain a vigorous MRI. Nonthermal ionization by stellar and accretion-driven X-rays and FUV radiation, and possibly also cosmic rays, may also allow an active MRI to develop at radii of $\gtrsim 30$ AU, although a recent ALMA study suggests that any turbulence in the outer disk may be quite weak (Flaherty et al. 2015). In any case it appears that there are large regions in protoplanetary disks where the MRI may not be able to transport enough mass to account for the observed values.

Armitage (2011) and Turner et al. (2014) provide excellent recent reviews of the highly complex problems of magnetic transport in dusty, cold protoplanetary disks. Here we sketch a few basic issues and recent results important for understanding observed disk accretion.

3.1. Magnetic Instabilities in Nonideal Magnetohydrodynamics

The first attempt to explain inward mass transport in the intermediate $\sim 0.3\text{--}30$ AU regions of low-ionization disks was that of Gammie (1996), who considered MRI-active layers of surface density Σ_a with a magnetically inert (dead) zone sandwiched in between. The accretion rate is then set by the mass transport at the boundary between the active layers and the fully active inner disk, $\dot{M} \approx 3\pi c_s^2 \alpha \Sigma_a \Omega^{-1}$. Assuming only Ohmic diffusion and a full cosmic ray flux, Gammie showed that the resulting surface density, $\Sigma_a \approx 100 \text{ g} \cdot \text{cm}^{-2}$, with a plausible viscosity parameter $\alpha \approx 10^{-2}$, would be enough to sustain a mass accretion rate of $\sim 10^{-8} M_{\odot} \cdot \text{year}^{-1}$.

There are, however, significant difficulties with this picture. Low-energy cosmic rays, which would be responsible for most of the ionization, may be excluded from the disk because of magnetized outflows (e.g., Cleeves et al. 2015). Stellar X-rays penetrate to a much smaller depth than cosmic rays, although possibly enough to sustain a significant turbulent accretion rate. But the biggest problem for sustaining MRI turbulence appears to be ambipolar diffusion (AD). The inclusion of AD in numerical simulations of intermediate disk regions limits the surface density with adequate coupling of ions and neutrals to $\sim 0.1\text{--}1 \text{ g} \cdot \text{cm}^2$, driven by FUV ionization

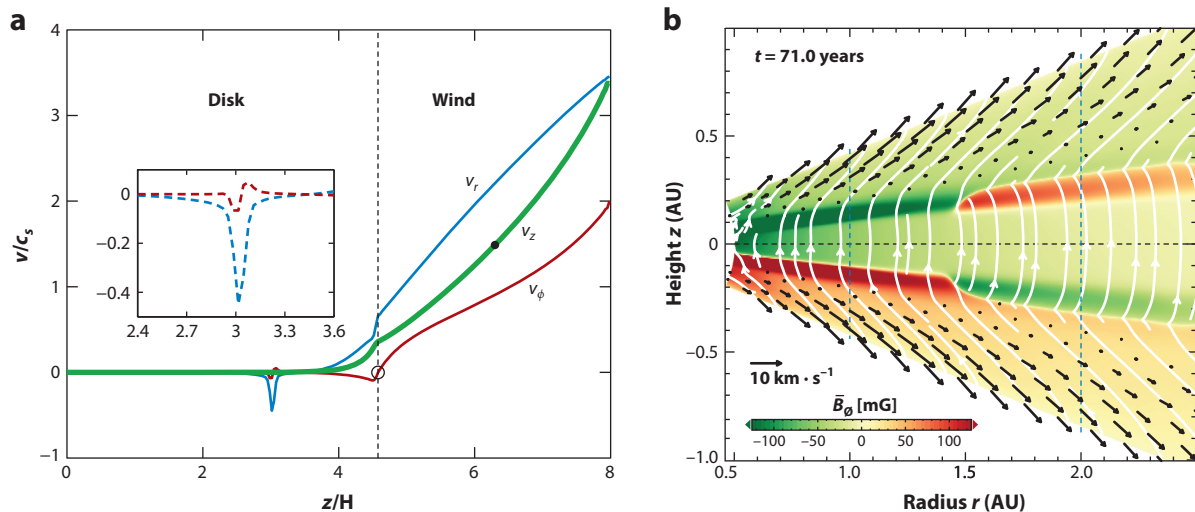


Figure 12

(a) Flow structure in a disk simulation with ambipolar diffusion (AD). A wind is driven in the outer disk layers, resulting in a laminar disk structure with a narrow accreting layer (see *inset*). Panel *a* adapted from Bai & Stone (2013) with permission. The velocities in the radial (r), vertical (z), and azimuthal (ϕ) directions are given in units of the sound speed c_s as a function of height above the disk midplane z in units of the scale height H . (b) Global simulation of a disk with AD, showing the overall flow pattern of the wind. The field bends outward, accelerating a wind that removes angular momentum, allowing disk material to move inward. Panel *b* adapted from Gressel et al. (2015) with permission.

(Perez-Becker & Chiang 2011; see also **Figure 12a**). This is far too small an active layer to sustain the necessary mass accretion into the inner MRI-active disk. Instead, simulations with AD suggest that transport is driven by magnetically driven disk winds (Bai & Stone 2013, Bai 2014, Gressel et al. 2015). A further complication is introduced by the Hall effect, which is also likely to be important in this region of the disk (see Wardle & Salmeron 2012 and references therein). We consider each of these effects in turn.

3.2. Disk Winds

Angular momentum loss by winds from protoplanetary disks was suggested long ago by Pudritz & Norman (1983); detailed analytic models of disks with AD were presented in a prescient paper by Königl (1989). Magnetic field lines threading the disk can force gas in the upper disk layers to corotate with the field footpoints. If the field lines then bend outward by more than a critical angle, the increased azimuthal velocity relative to the local Keplerian motion creates a centrifugal acceleration strong enough to overcome gravity, resulting in effective driving of a wind (Blandford & Payne 1982). The magnetic coupling between disk and wind then transfers angular momentum outward, allowing disk matter to accrete. This mechanism has been used to explain the bipolar jets of young stars (Bally 2016), which have velocities of $\gtrsim 100 \text{ km} \cdot \text{s}^{-1}$ that most likely require an origin in the innermost, rapidly rotating disk. Beyond the Alfvén surface, the magnetic field winds up, producing a toroidal field that helps collimate the flow into jets.

Simulations by Bai & Stone (2013) and Gressel et al. (2015) of disks with AD show the development of strong disk winds over a range of radii between ~ 1 and 10 AU, with angular momentum transport driven by wind coupling. The MRI is suppressed in these calculations, resulting in

a laminar disk. **Figure 12b** shows the geometry of characteristic magnetic field lines in these numerical simulations. The presence of AD allows the gas to diffuse past the field lines in dense regions, while the well-coupled gas in the upper layers of the vertically stratified disk lags behind, creating the desired field configuration for outflow (Königl 1989, Königl et al. 2010). Because the main section of the disk is not coupled effectively to the magnetic field, accretion does not occur except in a narrow layer where intermediate coupling allows the gas to lose angular momentum to the wind while still being able to diffuse inward past the field lines. The large accretion rates are then a result of fast inward velocities approaching the sound speed in this layer of small surface density (Bai & Stone 2013). Bai (2014) has argued that this is the dominant mode of mass and angular momentum transport in T Tauri disks at radii of ~ 1 – 10 AU, with thermal and nonthermal activation of MRI at smaller and larger radii, respectively.

These numerical simulations are not able to determine wind mass and angular momentum loss rates accurately because of computational limitations. It is therefore useful to consider some general requirements. If a wind carries off all the angular momentum needed to accrete through a unit radial length of a Keplerian disk at cylindrical radius R , then

$$\dot{M}_a \frac{GM}{2R} dR = \dot{m}_w (GM R)^{1/2} \left(\frac{R_A}{R} \right)^2 dR, \quad (13)$$

where \dot{M}_a is the accretion rate at R , \dot{m}_w is the mass loss rate per unit length, and R_A is the Alfvén radius of the magnetically accelerated flow. Because the energy loss in the wind is $\Omega = (GM/R^3)^{1/2}$ times the angular momentum loss rate, Equation 13 corresponds to the wind carrying off all the locally generated accretion energy (Königl 1989, Hartmann 2009).

Suppose for simplicity we set \dot{M}_a and $\eta \equiv (R_A/R) \approx$ constant; then, integrating to find the total wind mass loss rate, we obtain $\dot{M}_w = \int_{R_0}^{R_i} \dot{m}_w dR = (2\eta^2)^{-1} \dot{M}_a \ln(R_0/R_i)$. But the mass loss rate cannot exceed $\dot{M}_w \leq (2\eta^2)^{-1} \dot{M}_a$ because the wind would carry away more energy than is released by accretion. Typical wind models show modest values of $\eta \approx 3$ (see, for example, **Figure 12**), in which case moving mass inward by wind transport over more than an order of magnitude in radius is not consistent with a steady state.

Current estimates of winds/jets from low-mass pre-main-sequence stars (Calvet 2004, Natta et al. 2014) suggest that $\dot{M}_w \approx 10^{-1} \dot{M}_a$, with terminal velocities also requiring modest values of η . Note that this applies to observations of inner-disk winds; mass loss rates for the low-velocity flows seen in T Tauri forbidden lines of [OI] and [NeII] (Hartigan et al. 1995, Rigliaco et al. 2013; see also **Figure 6**) are extremely uncertain, and arguably might represent photoevaporative flows (Owen et al. 2011, Rigliaco et al. 2013) rather than (or in addition to) magnetically accelerated disk winds.

In the case of magnetospheric accretion, the angular momentum added to the star is $\Omega_0 R_{co}^2$, so the added rotational energy is approximately $\Omega_0^2 R_{co}^2 \approx GM_*/R_{co}$. Thus the luminosity problem (Section 4.2) cannot be solved by putting most of the released gravitational energy into the disk wind if magnetospheric accretion is occurring.

3.3. Hall Effect

Although the potential importance of the Hall effect in protoplanetary disks has been recognized for some time (Wardle 1999, Balbus & Terquem 2001, Kunz 2008), it has only recently been included in time-dependent numerical simulations (Lesur et al. 2014; Bai 2014, 2015; Simon et al. 2015). These simulations show that when the (vertical) magnetic field and the sense of rotation are parallel (i.e., $B \cdot \Omega > 0$), the Hall shear instability produces a very strong horizontal field with

large Maxwell stresses, enabling strong mass and angular momentum transport. The flow in the disk becomes laminar and the increase in the magnetic field causes a substantial increase in the disk vertical scale height. The MRI and winds may be enhanced in this situation. When $B \cdot \Omega < 0$, the horizontal field is suppressed and other instabilities are weakened, but when dissipation from AD is small, bursts of turbulence are seen.

In addition to the strong dependence on the alignment of the magnetic field and the sense of rotation, the levels of turbulence and transport depend sensitively on the assumed disk chemistry. Thus, at the moment there is no robust theory for protoplanetary disk accretion, and different processes likely dominate in differing regions of disks: thermally activated MRI turbulence in innermost regions; perhaps mostly wind-driven accretion at a few AU, and/or the Hall effect; and perhaps nonthermally ionized MRI at large radii. Such a combination of differing transport mechanisms suggests that mass flows through the disk are unlikely to be steady.

3.4. Gravitational Instability

Mass and angular momentum transport by GI is discussed in detail in the review by Kratter & Lodato (2016). Here we briefly note the potential relevance of GI for pre-main-sequence accretion.

Generally speaking, for gravitationally induced spiral waves to produce effective transport, the Toomre parameter $Q = c_s \kappa / \pi G \Sigma$ must be $\lesssim 1.4$, where the epicyclic frequency κ may be approximated by the Keplerian value Ω , and Σ is the surface density of the disk. As c_s , Ω is a strongly decreasing function of increasing cylindrical radius R , GI transport is more likely to be important at large radii. For typical disk parameters, this constraint on Q can be satisfied only with a disk mass that is substantial compared with the central star: $M_d / M_* \approx 0.1$. Most estimates of T Tauri disk masses, derived from (sub)millimeter-wave dust emission, are an order of magnitude lower than this (Williams & Cieza 2011), although these values basically represent the mass in about millimeter-sized particles, and might therefore be considered as lower limits.

GI transport is most likely to be relevant in the early protostellar phases. Infall rates of $\gtrsim 10^{-6} M_\odot \cdot \text{year}^{-1}$ are much higher than typical T Tauri accretion rates and are unlikely to be sustained by the disk winds discussed above, especially if the infalling matter extinguishes the FUV radiation thought to be important for ionizing the upper disk layers. Pileup of disk mass might then occur unless some alternative transport mechanism is available. However, the GI might produce sufficient heating in the inner disk that the MRI could be thermally activated, potentially leading to outbursts (Armitage et al. 2001, Zhu et al. 2009b; see also Section 4.2). In support of this picture, if the pre-outburst FU Ori disk at $R \approx 1$ AU (the estimated scale of the outburst region; see Section 2.4) is marginally unstable for a temperature of ~ 200 K and a central mass of $0.3 M_\odot$, the required surface density $\Sigma \approx c_s \Omega / (1.4 \pi G)$ would imply an inner-disk mass of $\pi R^2 \Sigma \approx 0.01 M_\odot$, comparable to the mass that has been accreted onto the central object.

4. PROTOSTELLAR INFALL AND ACCRETION

4.1. Observational Estimates of Protostellar Luminosities and Lifetimes

The ultraviolet-optical accretion continua discussed in Section 2 are usually not detectable in protostars with dusty opaque envelopes, although red-IR-continuum excesses have been studied in a few individual sources (Section 4.3). The most generally available constraints on protostellar accretion thus come from total system luminosities, assuming that the dusty envelope absorbs most of the radiant energy and re-emits this at (far)-IR wavelengths.

The sensitivity and improved spatial resolution of *Spitzer* have made possible larger and more refined surveys of protostellar properties than early studies using the Infrared Astronomical

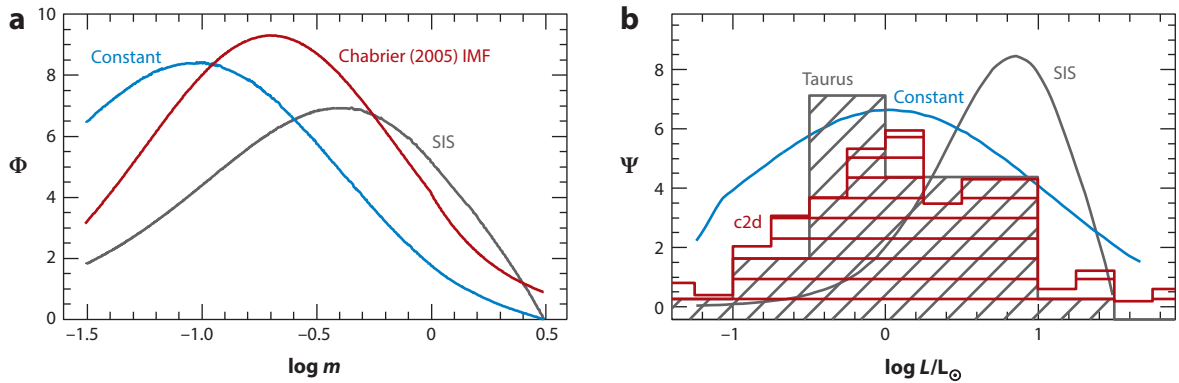


Figure 13

(a) Protostellar mass functions (PMFs) $\Phi = dN/d(\log m)$, where $m = M/M_{\odot}$, for the singular isothermal sphere (SIS) accretion model (gray line) and for a model in which all stars form in the same (constant) time (blue line), compared with the Chabrier (2005) initial mass function (IMF) (red line). The vertical axis is in arbitrary units. (b) Protostellar luminosity functions (PLFs) $\Psi = dN/d(\log L/L_{\odot})$ for the corresponding mass accretion models, compared with the observed PLFs in Taurus (Furlan et al. 2008) (gray-striped areas) and in the From Molecular Cores to Planet-Forming Disks (c2d) plus Gould’s Belt *Spitzer* Legacy Programs (Dunham et al. 2013) (red-striped areas). The assumed accretion rates are $2 \times 10^{-6} (M/0.4M_{\odot})^j M_{\odot} \cdot \text{year}^{-1}$, with $j = 0, 1$ (for the SIS and constant-time models, respectively), $\eta = 0.5$, and an upper mass limit of $3 M_{\odot}$.

Satellite (IRAS) (Wilking et al. 1989, Kenyon et al. 1990, Kenyon et al. 1994). These newer studies indicate that the median protostellar luminosity function in the low-mass star-forming regions peaks at about $1 L_{\odot}$ (Evans et al. 2009, Dunham et al. 2013), remarkably similar to the luminosity function found by Kenyon et al. (1990, 1994) for Taurus protostars (Figure 13). Although Dunham et al. (2013) suggest that unobserved emission at longer (submillimeter) wavelengths might increase luminosity estimates by a factor of two, the peak of the observed luminosity function is not far above the approximate completeness limits, suggesting that existing samples undercount very low luminosity objects (VeLLOs; Young et al. 2004, Bourke et al. 2006).

In principle, the timescales of protostellar collapse place additional constraints on accretion rates. Protostellar lifetimes are usually estimated by assuming steady-state star formation; the protostellar lifetime t_f is then given by the ratio of the number of protostars N_p to the number of young stellar objects $N_* = N(\text{Class II}) + N(\text{Class III})$ times the typical age of the young stellar population:

$$t_f \approx t_* N_p / N_* \quad (14)$$

(see the sidebar Spectral Energy Distribution Classes). Although t_* is a matter of some controversy, the typically adopted value of ~ 2 Myr seems reasonable for nearby actively star-forming regions (Kenyon et al. 1990, 1994).

The From Molecular Cores to Planet-Forming Disks (c2d) and Gould’s Belt *Spitzer* Legacy Programs (Evans et al. 2009, Dunham et al. 2013, 2015) have found significantly longer protostellar lifetimes ($t_f \approx 0.5$ Myr) compared with the original estimates (~ 0.1 – 0.2 Myr) of Kenyon et al. (1990, 1994). The *Spitzer* lifetimes might be somewhat overestimated because Class III (nonexcess) stars tend to be undercounted by IR surveys but can constitute a large fraction of young stellar populations (Kenyon et al. 1990, 1994, Haisch et al. 2001, Hernández et al. 2007). Protostar numbers might be inflated if large ambient extinctions make Class II stars look like protostars (van Kempen et al. 2009, McClure et al. 2010, Carney et al. 2015); however, low-luminosity protostars might go undetected. A final uncertainty is that the steady-state approximation may

SPECTRAL ENERGY DISTRIBUTION CLASSES

The spectral energy distribution (SED) classes of pre-main-sequence objects are based on the spectral slope in the near- to mid-IR wavelength region, which indicates the amount of dusty emission (and extinction). Class I objects are thought to be (mostly) protostars with such extensive dusty envelopes that mid- to far-IR emission dominates the SED. Class II objects have moderately strong IR excesses with decreasing fluxes toward longer wavelengths, consistent with emission essentially from systems with (opaque) dusty disks. Class III objects are pre-main-sequence stars with little or no IR excess and thus no optically thick disk emission. The low-mass Class II objects generally correspond to CTTS and the Class III stars to WTTS (see the sidebar *Accretion Versus Stellar Magnetic Activity*), consistent with disk accretion driving the excess optical and ultraviolet emission. The Class 0 type was added later to represent protostars with extremely large extinction and submillimeter emission; they are generally assumed to represent an earlier protostellar phase than Class I objects, although effects of viewing angle in systems with nonspherical envelopes can make Class I objects look like Class 0 if observed disk-edge-on, or like Class II if viewed along an outflow cavity. Although disk clearing eventually turns Class II stars into Class III objects, there are significant numbers of Class III stars with the same ages as Class II even at ages as young as 1–2 Myr.

not generally be valid (Offner & McKee 2011). The most likely conclusion is that (low-mass) protostellar lifetimes are probably somewhere between 0.3 and 0.6 Myr. Although uncertain, these estimates have implications for theories of protostellar collapse (Section 4.2).

4.2. The Luminosity Problem

The formation of a protostar from a much larger cold cloud requires a loss of energy given by its binding energy, which in standard models of accretion is mostly radiated away. Kenyon et al. (1990, 1994) found that standard models predicted much higher accretion luminosities than observed in the Class I objects in the Taurus molecular cloud. They suggested that the discrepancy could be explained by highly time-variable accretion, where much of the mass was accreted in short bursts like those of FU Ori objects (Section 2.5), so that most protostars are observed in a low-accretion, low-luminosity state (see also Vorobyov & Basu 2005, 2010, 2015, Bae et al. 2013, 2014). The existence of a luminosity problem was supported by the later *c2d Spitzer* Legacy Program results (Evans et al. 2009, Dunham et al. 2010). However, Offner & McKee (2011) and Myers (2011, 2014) constructed models of protostellar accretion without (significant) outburst that show no discrepancy between observed and predicted luminosities.

The protostellar luminosity function (PLF) depends in a complex way on the protostellar mass function (PMF), on the dependence of accretion rates on time and central mass, and even on whether the star formation rate is constant or perhaps accelerating (Offner & McKee 2011). However, the basic issues can be assessed using simple models. First, the radius-mass relation for the protostar is needed to convert an accretion rate into a luminosity. We adopt a simple fit of the protostellar radius for $<1 M_{\odot}$ objects of $R_* \approx 2.1(M_*/M_{\odot})^{0.25} R_{\odot}$, motivated by a few estimates of protostellar radii, along with limits from optically visible young stars and theoretical models (Section 4.4; see also Hartmann 2009, Offner & McKee 2011). The accretion luminosity is

$$L_{\text{acc}} = \eta GM_* \dot{M} / R_* \approx 8 \eta M_{0.3}^{1.75} \dot{M}_{-5.7} L_{\odot}, \quad (15)$$

where $\eta \leq 1$ is the fraction of the accretion energy radiated, $M_{0.3}$ is the protostellar mass in units of $0.3 M_{\odot}$, and $\dot{M}_{-5.7}$ is the mass accretion rate in units of $2 \times 10^{-6} M_{\odot} \cdot \text{year}^{-1}$. This fiducial

protostellar accretion rate, much higher than observed in T Tauri stars, corresponds to the infall rate predicted by the canonical singular isothermal sphere model for $T \approx 10$ K (Shu 1977), and would permit the formation of a $1-M_{\odot}$ star in 0.5 Myr.

Equation 15 shows that the accretion luminosity for a given mass accretion rate is sensitive to the protostellar mass. The PLF will then be set by the present-day PMF. In general the PMF will not be identical to the post-protostellar accretion initial mass function (IMF), and these differences will show up in the PLF.

Assume steady-state formation such that stars of a given final mass are produced at a rate consistent with the IMF. We then consider two simple models of accretion. The first is the singular isothermal sphere (SIS) model (Shu 1977), in which the accretion rate is constant in time and determined by the sound speed c_s as $\dot{M} = c_s^3/G \approx 2 \times 10^{-6} M_{\odot} \cdot \text{year}^{-1}$ for $T \approx 12$ K. This model predicts that the time to form a star is proportional to its final mass, which leads to a PMF that is skewed toward higher masses (**Figure 13a**); i.e., there are more higher-mass protostars because they take longer to form (McKee & Offner 2010). In turn, this leads to a PLF that is not only too luminous on average but is skewed toward high L_{acc} , inconsistent with observed distributions (**Figure 13b**; see also Offner & McKee 2011).

Given this result, an obvious alternative model to try is one in which all stars take the same time to form, i.e., $\dot{M} \propto M_f$. In this case the PMF has the same form as the IMF but shifted downward in mass by a factor of two (**Figure 13**). The resulting PLF is also shifted to lower values, with a shape in better agreement with observations. Further improvements can be made by lowering the fiducial mass accretion rate and letting the accretion rate decay with time (front-loading the mass addition at smaller masses; see Offner & McKee 2011, Myers 2014).

Thus, although Offner & McKee (2011) and Myers (2011, 2014) adopt different values for η and t_f and more complicated time dependences of accretion than used by Kenyon et al. (1990, 1994), the main reason why their PLF does not require outbursts is that their successful models produce low typical protostellar masses, with median values $\sim 0.1 M_{\odot}$, and with a significant number of protostellar brown dwarfs contributing to the low-luminosity end of the PLF (**Figure 13**).

The suggestion that $t_f \propto M_f$ is not consistent with observations has interesting implications for protostellar core structure—if, of course, the protostellar accretion rates are equal to the infall rates. For example, the collapse timescale of a (near-critical) Bonnor–Ebert (BE) sphere, which is probably a more realistic model of a thermally supported protostellar cloud core (e.g., Alves et al. 2001), also scales in the same way as the SIS model. The (critical) BE sphere collapse exhibits a decreasing infall rate with time (Foster & Chevalier 1993), but this does not lower the peak of the PLF sufficiently to compensate for the weighting of the PMF to higher masses. Conversely, if higher-mass stars must form in similar times, this raises problems for theories in which protostellar cores are the result of thermally-supported Jeans mass fragmentation (an example of which is the critical BE sphere), suggesting that the protostellar cloud core mass function does not map directly into the stellar IMF (see also Myers 2014). Numerical simulations have been employed to address protostellar luminosities for possibly more realistic (dynamic) initial conditions (Hansen et al. 2012, Padoan et al. 2014), but as they cannot resolve scales near the stellar radius, where most of the accretion luminosity will be radiated, their applicability is not clear.

Although determining protostellar properties is usually quite difficult owing to high extinction, it may be possible to measure protostellar masses from the kinematics of infalling envelopes and/or circumstellar disks (Tobin et al. 2012, Murillo et al. 2013, Ohashi et al. 2014) and thus provide a robust test of these models. This is especially important as one might surmise that observations are likely to be biased toward higher-luminosity (and thus higher-mass) protostars.

4.3. Direct Estimates of Protostellar Accretion Rates

Given the difficulties in theoretically explaining T Tauri mass accretion rates of only $10^{-8} M_{\odot} \cdot \text{year}^{-1}$ discussed in Section 3, it is not at all obvious that disk accretion can keep up with infall (Kenyon et al. 1990) as assumed in the PLF models of the previous section. Even if gravitational instabilities limit the amount of mass that can be piled up in the disk, it is not clear that they can produce transport all the way down to the star (Section 3.3). In addition, the models of the PLF have many uncertain parameters. It is therefore important to estimate protostellar accretion rates directly when possible.

In some cases the red and near-IR spectra of the central protostar can be directly detected and analyzed. Assuming steady spherical infall at free-fall velocities and typical interstellar medium dust opacities, the optical depth to the central object at $\lambda \approx 1 \mu\text{m}$ is

$$\tau_{1\mu\text{m}} \approx 2\dot{M}_{-5.7} M_{0.3}^{-1/2} R_{i,100}^{-1/2}, \quad (16)$$

where $\dot{M}_{-5.7}$ is the infall rate to the star and disk in units of $2 \times 10^{-6} M_{\odot} \cdot \text{year}^{-1}$, $M_{0.3}$ is the central mass in units of $0.3 M_{\odot}$, and $R_{i,100}$ is a characteristic disk radius at which the infall lands in units of 100 AU. In the case of the Terebey et al. (1984) model for rotating collapse, identifying R_i with the centrifugal radius—the outer region where mass lands on the disk—the optical depth would be about a factor of two larger.

Equation 16 indicates that it should be possible to detect near-IR protostellar properties for plausible infall rates if the inner-disk cavity (owing presumably to the formation of a disk) is large enough. This requirement is lessened by the presence of outflow cavities in the protostellar envelope, where radiation can escape much more easily. Many of the following studies, particularly those at shorter wavelengths, rely on observing the central object in scattered light rather than directly through the extinguishing envelope.

The most sensitive optical survey of protostars is that of White & Hillenbrand (2004), who studied 15 Class I sources in Taurus in the red-optical region. On the basis of estimates of continuum excess (veiling), and adopting the usual bolometric corrections, they inferred accretion rates of only $\sim 10^{-7} M_{\odot} \cdot \text{year}^{-1}$, suggesting that accretion rates are indeed lower than infall rates. White & Hillenbrand suggested that these Class I objects might not be in the main phase of protostellar mass accretion, but at the end of envelope infall with essentially their final masses. This does not solve the luminosity problem, however, because the Class 0 phase is considerably shorter than the Class I lifetime, as inferred from relative numbers, so accretion luminosities should be much greater than observed (Evans et al. 2009).

The difficulty of observing ultraviolet-optical continuum excesses in protostars led to efforts to calibrate IR emission lines with accretion rates, as discussed in Section 2.4.1. Applying this calibration to a small sample of Class I protostars in the Ophiuchus star-forming region, Muzerolle et al. (1998) found accretion luminosities somewhat higher than those of typical T Tauri stars but, at $\sim 10^{-7} M_{\odot} \cdot \text{year}^{-1}$, well below typical infall rates, and consistent with the existence of a luminosity problem (White et al. 2007). Although Nisini et al. (2005) and Caratti o Garatti et al. (2012) found a few objects with estimated accretion rates $\gtrsim 10^{-6} M_{\odot} \cdot \text{year}^{-1}$, most were consistent with the results of Muzerolle et al. (1998). Salyk et al. (2013) extended these efforts using the $\text{P}\beta$ emission lines—advantageous because smaller extinction corrections are needed—and again estimated modest accretion luminosities and rates.

These IR protostellar emission lines, with velocity widths in protostars typical of those seen in T Tauri stars (Doppmann et al. 2005), are consistent with a picture in which magnetospheric accretion at somewhat elevated rates is typical in the early phases of low-mass star formation. A

caveat is needed here: The physical basis for line luminosity versus total accretion luminosity is not as clear as for accretion shocks, and strong winds may have a larger contribution to line emission at young ages.

Doppmann et al. (2005) obtained high-resolution near-IR spectra of protostars (Class I and flat-spectrum) in Taurus, Ophiuchus, and Serpens, enabling them to estimate effective temperatures. Placing these objects in a Hertzsprung–Russell diagram is difficult because of extinction and uncertain contributions of scattered light. However, the results suggest similar radius–luminosity relations as for Class II objects. More significantly from the point of view of the luminosity problem, the spectral types span a range suggestive of masses between about 0.3 and 1 M_{\odot} . Similarly, in a near-IR study of Class I protostars at lower spectral resolution, Connelley & Greene (2010) found a range of spectral types, but not a preponderance of late M-type stars. Although these studies have an observational bias toward brighter objects, they strongly indicate that $M > 0.3 M_{\odot}$ protostars are a significant fraction of the population. Caratti o Garatti et al. (2012) found similar protostellar properties in the L1641 (Orion A) cloud. In view of the strong dependence of the accretion luminosity per unit accretion rate on the protostellar mass (Equation 15), these results suggest that the luminosity problem may still exist for many objects, especially as estimates of envelope infall rates in a very few protostars can be as large as $\gtrsim 10^{-4}$ – $10^{-5} M_{\odot} \cdot \text{year}^{-1}$ (Di Francesco et al. 2001, Belloche et al. 2006, Mottram et al. 2013).

4.4. Effects of Accretion on Protostellar Properties and Pre-Main-Sequence Stellar Ages

Ages of pre-main-sequence stars are conventionally calculated assuming gravitational contraction from very large initial radii (with a small contribution from deuterium fusion). However, it has been known since the work of Larson (1969) that protostellar collapse is far from homologous, and that at the end of major mass infall stars have relatively small radii ($\sim 3 R_{\odot}$ at 1 M_{\odot}). Thus, the usual evolutionary tracks provide upper limits to the ages of young stars. Apart from other uncertainties (mainly getting the stellar mass right; see, e.g., Soderblom 2010, Soderblom et al. 2014), accurate ages for young stars depend upon choosing the correct initial radius at the end of infall from which to start the contraction calculations.

The crucial factor in determining the initial stellar radius is the amount of thermal energy that is trapped during infall, which in turn depends upon the treatment of radiative losses. Following the spherical hydrodynamic treatment of Larson (1972), later studies have included more detailed opacities and rotation (e.g., Bate 2010, Schönke & Tscharnuter 2011, Vaytet et al. 2013). Unfortunately, it has proved difficult to follow the hydrodynamic treatment for long enough to build up a protostellar core with a sizable fraction of the initial cloud mass. This problem has led to studies in which an initial hydrostatic core of a specific mass and radius is assumed, allowing longer-term calculations of the core evolution in spherical accretion using modified stellar evolutionary methods (Stahler et al. 1980, Stahler 1988, Palla & Stahler 1991, Hosokawa et al. 2011). Although there is reasonable agreement among these studies, the final radius at the end of accretion does show a modest dependence upon the infall rate and initial radius of the hydrostatic core (Stahler 1988). However, most of the final mass is probably accreted from disks; the distinction between these phases is important because photons can escape more readily from disk geometry than from spherical geometry, resulting in the addition of colder material than for spherical infall (Hartmann et al. 1997).

The amount of thermal energy added to a protostar during disk accretion is uncertain. However, it is likely that such energy addition is relatively modest for thin disks or magnetospheric accretion (Hartmann et al. 1997), so as a first approximation we can assume cold mass addition. The evolution

of a fully convective protostar is then governed by (Hartmann et al. 1997)

$$\frac{\dot{R}_*}{R_*} \approx \frac{7}{3} \frac{R_*}{GM_*^2} \left[-L_* + \left(\beta_D - \frac{GM_*}{7R_*} \right) \dot{M} \right], \quad (17)$$

where L_* is the photospheric luminosity of the surface of the star unaffected by the presence of the disk (or accretion shock). The first term on the right produces the usual pre-main-sequence contraction owing to radiative losses; in the second term we have made the simplifying assumption that deuterium is mixed fully in the star as it is added and fused at a steady rate, with an energy release of β_D per gram.

Equation 17 shows that in the absence of deuterium fusion, the addition of cold mass makes the star contract faster. When deuterium burning is important, its sensitive temperature dependence tends to keep the central temperature $T_c \propto M_*/R_*$ constant. This leads to a common $R_*(M_*)$ relation (Stahler 1988), and the evolutionary tracks line up or overlap independent of mass accretion rate or initial conditions, as shown in the lower sections of the tracks (Hartmann et al. 1997) in **Figure 14** (*red solid curves*). However, when $L_* > \beta_D \dot{M}$, the deuterium energy release cannot keep up with the photospheric energy loss, and the evolutionary tracks fall below the $R_* \propto M_*$ sequence. The photospheric luminosity at which this occurs depends upon the mass accretion rate, leading to a range of radii for stars of a given mass at the end of major accretion.

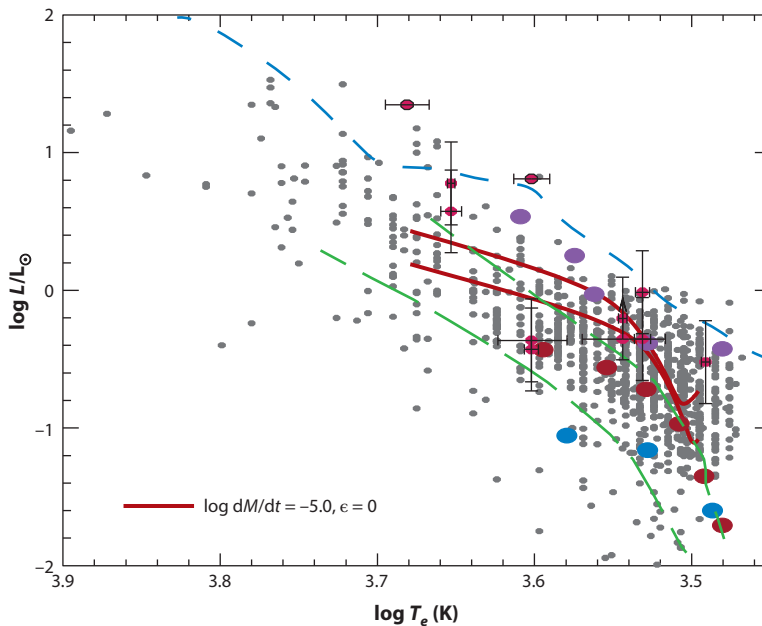


Figure 14

Evolutionary tracks of protostars under different assumptions, compared with the Hertzsprung–Russell diagram positions of young stars in the Orion Nebula Cluster (Da Rio et al. 2014) (*gray dots*) and Taurus protostars (Doppmann et al. 2005) (*magenta dots with error bars*). (The two brightest protostars are systems where accretion dominates the luminosity.) The blue dashed curve is the result of Palla & Stahler (1999) for spherical accretion at $\dot{M} = 10^{-5} M_{\odot} \cdot \text{year}^{-1}$. The two solid red curves are the results of Hartmann et al. (1997) for two different initial radii at $0.1 M_{\odot}$: 1.5 and $1 R_{\odot}$. Also shown are positions of evolutionary tracks from Hosokawa et al. (2011) for cold accretion starting from $0.3 R_{\odot}$ and $0.035 M_{\odot}$ (*blue dots*) and $1.5 R_{\odot}$ and $0.074 M_{\odot}$ (*red dots*), as well as for extended hot accretion up to $0.03 M_{\odot}$ followed by cold accretion (*purple dots*). The two green long-dashed curves are isochrones at 1 and 10 Myr from Baraffe et al. (2015).

Further spreads in protostellar properties can be produced by changing the initial radius and/or mass at the beginning of disk (cold) accretion. Assuming a larger initial radius, placing the protostar above the deuterium fusion main sequence (**Figure 14**) allows the protostar to contract until deuterium fusion may (or may not) become important. Conversely, starting with a small initial radius can lead to a particularly small protostar at the end of significant accretion (**Figure 14**) if $R_* < GM/(7\beta_D)$, so that the addition of negative potential energy overcomes that available from deuterium fusion. This type of initial condition was used by Baraffe & Chabrier (2010) and Baraffe et al. (2012) in an attempt to explain observations of objects in star-forming regions that appear to be much older than the bulk of the population.

It is difficult to use estimates of protostellar properties to test these possibilities given observational uncertainties (Soderblom et al. 2014). However, comparison with the optically visible young star population can be used to place constraints on properties, assuming that these stars have not contracted very far from their initial (final protostellar) radii. The comparison in **Figure 14** indicates that initial conditions such that deuterium fusion is significant (including time-averaged accretion rates of $\sim 10^{-6}$ – $10^{-5} M_\odot \cdot \text{year}^{-1}$) are in rough agreement with observations for lower-mass stars; completely spherical accretion (blue dashed curve in **Figure 14**) seems to result in radii that are somewhat too large. Conversely, cold accretion starting from small radii is not consistent with most of the population. However, within these broad conclusions it is apparent that plausible variations in initial conditions lead to great uncertainties in any attempt to estimate ages of ~ 1 Myr. Moreover, for stars with effective temperatures $T_e > 4,000$ K and/or luminosities $L_* > 1 L_\odot$, the calculations and observations indicate that canonical isochrones assuming contraction from large initial radii significantly overestimate ages (Hartmann 2003, Hosokawa et al. 2011).

One situation in which cold disk accretion may not be appropriate is at high accretion rates, which in general can only be sustained for short periods of time. Models for the outburst of FU Ori (Zhu et al. 2009b) indicate that at $\dot{M} \gtrsim 10^{-4} M_\odot \cdot \text{year}^{-1}$, the inner disk can become geometrically thick, with midplane temperatures approaching $T \approx 10^5$ K or more. In these circumstances the disk radiates much less efficiently; in addition, as the magnetosphere probably gets crushed against the star, a large fraction of the stellar photosphere is blocked by the opaque disk. This can lead to significant transport of heat into the star (Popham et al. 1996), which can then cause expansion of the star's outer layers, potentially explaining the large inner-disk radius inferred for FU Ori (Baraffe et al. 2012). It is not clear whether outbursting disk accretion affects the long-term evolution of a protostar or simply inflates the outer layers for a short period of time followed by relaxation as the excess energy is radiated away.

4.5. Implications for Planet Formation and Migration

As noted in Section 3, CTTS accretion rates and lifetimes indicate that a substantial fraction of disk mass is accreted on timescales of a few millions of years, implying inward transport of disk material from large distances. Toy models of fully viscous disks suggest that these constraints are consistent with an effective viscosity parameter $\alpha \approx 10^{-2}$ – 10^{-3} , with transport of material over ~ 100 AU occurring over timescales of 1–10 Myr (Hartmann et al. 1998). Such effective transport can be important in moving gap-opening giant planets inward during Type II migration (Kley & Nelson 2012, Baruteau et al. 2014). Of course, it is highly unlikely that protoplanetary disks are fully viscous (Section 3), and the differences in migration that might occur if winds and/or the Hall effect dominate the angular momentum and mass transport are not yet clear. Other structures in the disk density and temperature distribution that might arise owing to complex nonideal MHD transport can also have an effect on planet formation and migration, but this remains uncertain.

More generally, the finite lifetimes of protoplanetary disks obviously place constraints on the timescales of at least giant planet formation. Photoevaporation is likely to be the dominant effect

that ultimately removes disk gas (see, e.g., Owen et al. 2011 and references therein). However, the rapid decay of accretion (and dusty disk emission), although potentially compatible with photoevaporative models, might also indicate the formation of giant planets, which open gaps and thus prevent outer-disk material from replenishing the accreting inner-disk gas. Many uncertainties remain, but the observational advances that are being made in high-spatial resolution studies of disks give hope that progress can be made on at least some of these issues, providing the needed constraints for the increasingly sophisticated simulations of accreting protoplanetary disks.

SUMMARY POINTS

1. Nearly all pre-main-sequence stars of masses $\lesssim 1 M_{\odot}$, and at least some objects of masses up to $\sim 3 M_{\odot}$, accrete from their disks via funnel flows in stellar magnetospheres. Most of the energy of accretion is radiated by the accretion shock at the stellar surface, with only small amounts of thermal energy added to the star. The majority of the stellar mass is probably accreted from the disk in many if not most cases.
2. The mechanisms by which angular momentum is transported in protostellar and protoplanetary disks are not well understood at present. Gravitational instability is likely to be important only in the earliest stages of protostellar collapse. Recent studies deprecate the importance of the magnetorotational instability in large regions of these cold, low-ionization disks; alternatives are magnetically driven disk winds and winding of magnetic fields owing to the Hall effect.
3. Typical accretion rates for low-mass stars of $\sim 10^{-8} M_{\odot} \cdot \text{year}^{-1}$ lasting for $\sim 2\text{--}3$ Myr imply the accretion over time of order 10 Jupiter masses or nearly a minimum-mass solar nebula, comparable to the reservoirs of material estimated from millimeter- and submillimeter-wave emission from dusty disks.
4. Protostellar accretion is not well understood, but variations in initial conditions are likely to result in a range of stellar radii for a given mass at the end of the protostellar phase. This introduces considerable uncertainty in contraction ages of $\sim 1\text{--}2$ Myr for low-mass stars, and even more for intermediate-mass stars. Conventional pre-main-sequence isochrones assume contraction from much larger radii than typical of protostars, and therefore ages from these calculations must be systematically upper limits.

DISCLOSURE STATEMENT

The authors are not aware of any affiliations, memberships, funding, or financial holdings that might be perceived as affecting the objectivity of this review.

ACKNOWLEDGMENTS

We acknowledge helpful comments and/or figures from Silvia Alencar, Xuening Bai, Nancy Brickhouse, Ann Marie Cody, J.-F. Donati, Suzan Edwards, Scott Gregory, Oliver Gressel, Gaiete Hussain, Laura Ingleby, Moira Jardine, Ágnes Kóspál, Ryuichi Kurosawa, Doug Lin, Carlo Manara, Melissa McClure, Phil Myers, Stella Offner, and Zhaohuan Zhu. Final comments and suggestions were provided by Ewine van Dishoeck, Neal Evans, and Subu Mohanty. This review was supported in part by the University of Michigan and in part by grant 11473005 awarded by the National Science Foundation of China.

LITERATURE CITED

- Ábrahám P, Juhász A, Dullemond CP, et al. 2009. *Nature* 459:224
- Acke B, van den Ancker ME, Dullemond CP. 2005. *Astron. Astrophys.* 436:209
- Adams FC, Gregory SG. 2012. *Ap. J.* 744:55
- Alcala JM, Natta A, Manara CF, et al. 2014. *Astron. Astrophys.* 561:2
- Alecian E, Wade GA, Catala C, et al. 2013. *MNRAS* 429:1001
- Alencar SHP, Batalha C. 2002. *Ap. J.* 571:378
- Alencar SHP, Boucher J, Walter FM, et al. 2012. *Astron. Astrophys.* 541:116
- Alencar SHP, Teixeira PS, Guimarães MM, et al. 2010. *Astron. Astrophys.* 519:88
- Alexander RD, Armitage PJ. 2009. *Ap. J.* 704:989
- Alexander R, Pascucci I, Andrews S, et al. 2014. See Beuther et al. 2014, pp. 475–96
- Alves JF, Lada CJ, Lada EA. 2001. *Nature* 409:159
- Antonucci S, García López R, Nisini B, et al. 2011. *Astron. Astrophys.* 534:32
- Antonucci S, García López R, Nisini B, et al. 2014. *Astron. Astrophys.* 572:62
- Ardila DR, Basri G. 2000. *Ap. J.* 539:834
- Ardila DR, Herczeg GJ, Gregory SG, et al. 2013. *Ap. J. Suppl.* 207:1
- Argiroffi C, Maggio A, Peres G. 2007. *Astron. Astrophys.* 465:L5
- Armitage PJ. 2011. *Annu. Rev. Astron. Astrophys.* 49:195
- Armitage PJ, Livio M, Pringle JE. 2001. *MNRAS* 324:705
- Aspin C, Reipurth B, Herczeg GJ, Capak P. 2010. *Ap. J.* 719:L50
- Audard M, Ábrahám P, Dunham MM, et al. 2014. See Beuther et al. 2014, pp. 387–410
- Bae J, Hartmann L, Zhu Z, Gammie C. 2013. *Ap. J.* 764:141
- Bae J, Hartmann L, Zhu Z, Nelson RP. 2014. *Ap. J.* 795:61
- Bagnulo S, Fossati L, Landstreet JD, Izzo C. 2015. *Astron. Astrophys.* 583:115
- Bai XN. 2014. *Ap. J.* 791:137
- Bai XN. 2015. *Ap. J.* 798:84
- Bai XN, Stone JM. 2013. *Ap. J.* 767:30
- Balbus SA, Hawley JF. 1998. *Rev. Mod. Phys.* 70:1
- Balbus SA, Terquem C. 2001. *Ap. J.* 552:235
- Bally J. 2016. *Annu. Rev. Astron. Astrophys.* 54. In press
- Banzatti A, Meyer MR, Bruderer S, et al. 2012. *Ap. J.* 745:90
- Banzatti A, Pontoppidan KM, Bruderer S, et al. 2015. *Ap. J.* 798:L16
- Baraffe I, Chabrier G. 2010. *Astron. Astrophys.* 521:A44
- Baraffe I, Homeier D, Allard F, Chabrier G. 2015. *Astron. Astrophys.* 577:A42
- Baraffe I, Vorobyov E, Chabrier G. 2012. *Ap. J.* 756:118
- Baruteau C, Crida A, Paardekooper S, et al. 2014. See Beuther et al. 2014, pp. 667–89
- Basri G, Batalha C. 1990. *Ap. J.* 363:654
- Basri G, Bertout C. 1989. *Ap. J.* 341:340
- Bate MR. 2010. *MNRAS* 404:L79
- Bayo A, Barrado D, Huelamo N, et al. 2012. *Astron. Astrophys.* 547:80
- Belloche A, Hennebelle P, André P. 2006. *Astron. Astrophys.* 453:145
- Beristain G, Edwards S, Kwan J. 2001. *Ap. J.* 551:1037
- Bertout C, Basri G, Bouvier J. 1988. *Ap. J.* 330:350
- Bessolaz N, Zanni C, Ferreira J, et al. 2008. *Astron. Astrophys.* 478:155
- Beuther H, Klessen RS, Dullemond CP, Henning TK, eds. 2014. *Protostars and Planets*, Vol. 6. Tucson: Univ. Ariz. Press
- Blandford RD, Payne DG. 1982. *MNRAS* 199:883
- Blinova AA, Romanova MM, Lovelace RVE. 2016. *MNRAS* 459:2354
- Bonito R, Orlando S, Argiroffi C, et al. 2014. *Ap. J. Lett.* 795:L34
- Bonnell IA, Smith KW, Meyer MR, et al. 1998. *MNRAS* 299:1013
- Bourke TL, Myers PC, Evans NJ II, et al. 2006. *Ap. J. Lett.* 649:L37
- Bouvier J, Alencar SHP, Boutelier T, et al. 2007. *Astron. Astrophys.* 463:1017

- Bouvier J, Grankin K, Ellerbroek LE, et al. 2013. *Astron. Astrophys.* 557:77
- Bouvier J, Matt SP, Mohanty S, et al. 2014. See Beuther et al. 2014, pp. 433–50
- Bowler BP, Liu M, Kraus AL, et al. 2011. *Ap. J.* 743:148
- Brickhouse NS, Cranmer SR, Dupree AK, et al. 2010. *Ap. J.* 710:1835
- Brickhouse NS, Cranmer SR, Dupree AK, et al. 2012. *Ap. J. Lett.* 760:L21
- Calvet N. 2004. In *Stars as Suns: Activity, Evolution and Planets. Proc. Symp. Int. Astron. Union, 219th, Sydney, July 21–25, 2003*, ed. AK Dupree, AO Benz, pp. 599–609. San Francisco: Astron. Soc. Pac.
- Calvet N, Basri G, Kuhl LV. 1984. *Ap. J.* 277:725
- Calvet N, Briceño C, Hernández J, et al. 2005. *Astron. J.* 129:935
- Calvet N, Gullbring E. 1998. *Ap. J.* 509:802
- Calvet N, Muzerolle J, Briceño C, et al. 2004. *Astron. J.* 128:1294
- Caratti o Garatti A, García López R, Antonucci S, et al. 2012. *Astron. Astrophys.* 538:A64
- Carney MT, Yildiz UA, Mottram JC, et al. 2015. *Astron. Astrophys.* 586:A44
- Cauley PW, Johns-Krull CM. 2014. *Ap. J.* 797:112
- Cauley PW, Johns-Krull CM. 2015. *Ap. J.* 810:5
- Chabrier G. 2005. In *The Initial Mass Function 50 Years Later*, ed. EE Salpeter, E Corbelli, F Palla, H Zinnecker, pp. 41–50. *Astrophys. Space Sci. Libr.* 327. New York: Springer
- Chen W, Johns-Krull CM. 2013. *Ap. J.* 776:113
- Cieza LA, Sreieiber MR, Romero GA, et al. 2010. *Astron. J.* 712:925
- Clarke CJ, Gendrin A, Sotomayor M. 2001. *MNRAS* 328:485
- Cleeves LL, Bergin EA, Qi C, et al. 2015. *Ap. J.* 799:204
- Cody AM, Stauffer J, Baglin A, et al. 2014. *Astron. J.* 147:82
- Cody AM, Hillenbrand LA. 2014. *Ap. J.* 796:129
- Connelley MS, Greene TP. 2010. *Astron. J.* 140:1214
- Costigan G, Scholz A, Stelzer B, et al. 2012. *MNRAS* 427:1344
- Costigan G, Vink JS, Scholz A, et al. 2014. *MNRAS* 440:3444
- Cottaar M, Covey KR, Meyer MR, et al. 2014. *Ap. J.* 794:125
- Covey KR, Hillenbrand LA, Miller AA, et al. 2011. *Astron. J.* 141:40
- Cranmer SR. 2008. *Ap. J.* 689:316
- Cranmer SR. 2009. *Ap. J.* 706:824
- D'Alessio P, Calvet N, Hartmann L, et al. 1999. *Ap. J.* 527:893
- D'Angelo CR, Spruit HC. 2010. *MNRAS* 406:1208
- D'Angelo CR, Spruit HC. 2012. *MNRAS* 420:416
- Da Rio N, Jeffries RD, Manara CF, Robberto M. 2014. *MNRAS* 439:3308
- Da Rio N, Robbero M, Hillenbrand LA, et al. 2012. *Ap. J.* 748:14
- Dahm SE. 2008. *Astron. J.* 136:521
- Di Francesco J, Myers PC, Wilner DJ, et al. 2001. *Ap. J.* 562:770
- Dodin AV, Lamzin SA. 2012. *Astron. Lett.* 38:649
- Donati JF, Gregory SG, Alencar SHP, et al. 2011. *MNRAS* 417:472
- Donati JF, Gregory SG, Alencar SHP, et al. 2012. *MNRAS* 425:2948
- Donati JF, Jardine MM, Gregory SG, et al. 2007. *MNRAS* 380:1297
- Donati JF, Landstreet JD. 2009. *Annu. Rev. Astron. Astrophys.* 47:333
- Donati JF, Morin J, Petit P, et al. 2008. *MNRAS* 390:545
- Donehew B, Brittain S. 2011. *Astron. J.* 141:46
- Doppmann GW, Greene TP, Covey KR, Lada CJ. 2005. *Astron. J.* 130:1145
- Drake JJ. 2005. In *Proc. Camb. Worksh., Cool Stars, Stellar Systems and the Sun, 13th, Hamburg, Ger., July 5–9, 2004*, ed. F Fatava, GAJ Hussain, B Battrick, pp. 519–22. Noordwijk, Neth: Eur. Space Agency
- Dullemond CP, Monnier JD. 2010. *Annu. Rev. Astron. Astrophys.* 48:205
- Dunham MM, Allen LE, Evans NJ II, et al. 2015. *Ap. J. Suppl.* 220:11
- Dunham MM, Arce HG, Allen LE, et al. 2013. *Astron. J.* 145:94
- Dunham MM, Evans NJ II, Terebey S, et al. 2010. *Ap. J.* 710:470
- Dupree AK, Brickhouse NS, Cranmer SR, et al. 2012. *Ap. J.* 750:73
- Dupree AK, Brickhouse NS, Cranmer SR, et al. 2014. *Ap. J.* 789:27

- Dupree AK, Brickhouse NS, Smith GH, Strader J. 2005. *Ap. J.* 625:L131
- Edwards S, Fischer W, Hillenbrand L, Kwan J. 2006. *Ap. J.* 646:319
- Edwards S, Fischer W, Kwan J, et al. 2003. *Ap. J. Lett.* 599:L41
- Edwards S, Kwan J, Fischer W, et al. 2013. *Ap. J.* 778:148
- Eisner JA, Monnier JD, Woillez J, et al. 2010. *Ap. J.* 718:774
- Ellerbroek LE, Podio L, Dougados C, et al. 2014. *Astron. Astrophys.* 563:87
- Esau CF, Harries TJ, Bouvier J. 2014. *MNRAS* 443:1022
- Espaillet C, Muzerolle J, Najita J, et al. 2014. See Beuther et al. 2014, pp. 497–520
- Evans NJ II, Dunham MM, Jørgensen JK, et al. 2009. *Ap. J. Suppl.* 181:321
- Fairlamb JR, Oudmaijer RD, Mendigutia I, et al. 2015. *MNRAS* 453:976
- Fang M, Kim JS, van Boekel R, et al. 2013. *Ap. J. Suppl.* 207:39
- Fang M, van Boekel R, Wang W, et al. 2009. *Astron. Astrophys.* 504:461
- Favata F, Flaccomio E, Reale F, et al. 2005. *Ap. J. Suppl.* 160:469
- Fedele D, van den Ancker ME, Henning Th, et al. 2010. *Astron. Astrophys.* 510:72
- Feiden G. 2016. *Astron. Astrophys.* In press. arXiv:1604.08036
- Ferreira J, Dougados C, Cabrit S. 2006. *Astron. Astrophys.* 453:785
- Fischer W, Edwards S, Hillenbrand L, Kwan J. 2011. *Ap. J.* 730:73
- Fischer W, Kwan J, Edwards S, Hillenbrand L. 2008. *Ap. J.* 687:1117
- Flaherty KM, Hughes AM, Rosenfeld KA, et al. 2015. *Ap. J.* 813:99
- Foster PN, Chevalier RA. 1993. *Ap. J.* 416:303
- Frank A, Ray TP, Cabrit S, et al. 2014. See Beuther et al. 2014, pp. 451–74
- Frasca A, Biazzo K, Lanzafame AC, et al. 2015. *Astron. Astrophys.* 575:4
- Furlan E, McClure M, Calvet N, et al. 2008. *Ap. J. Suppl.* 176:184
- Gahm GF, Walter FM, Stempels HC, Petrov PP. 2008. *Astron. Astrophys.* 482:L35
- Gammie CF. 1996. *Ap. J.* 457:355
- García López R, Natta A, Testi L, Habart E. 2006. *Astron. Astrophys.* 459:837
- Gómez de Castro AI, Lamzin SA. 1999. *MNRAS* 304:L41
- Goodson AP, Winglee RM, Böhm KH. 1997. *Ap. J.* 489:199
- Gorti U, Hollenbach D. 2009. *Ap. J.* 690:1539
- Grady CA, Hamaguchi K, Schneider G, et al. 2010. *Ap. J.* 719:1565
- Grady CA, Woodgate B, Torres CAO, et al. 2004. *Ap. J.* 608:809
- Grankin KN, Melnikov SY, Bouvier J, et al. 2007. *Astron. Astrophys.* 461:183
- Gregory SG, Donati JF, Morin J, et al. 2012. *Ap. J.* 755:97
- Gregory SG, Matt SP, Donati JF, Jardine M. 2008. *MNRAS* 389:1839
- Gressel O, Turner NJ, Nelson RP, McNally CP. 2015. *Ap. J.* 801:84
- Grosso N, Audard M, Bouvier J, et al. 2007. *Astron. Astrophys.* 468:557
- Güdel M, Nazé Y. 2010. *Space Sci. Rev.* 157:211
- Günther HM, Lewandowska N, Hundertmark MPG, et al. 2010. *Astron. Astrophys.* 518:54
- Günther HM, Schmitt JHMM. 2008. *Astron. Astrophys.* 481:735
- Günther HM, Schmitt JHMM, Robrade J, Liefke C. 2007. *Astron. Astrophys.* 466:1111
- Gullbring E, Calvet N, Muzerolle J, Hartmann L. 2000. *Ap. J.* 544:927
- Gullbring E, Hartmann L, Briceño C, Calvet N. 1998. *Ap. J.* 492:323
- Haisch KE Jr., Lada EA, Lada CJ. 2001. *Ap. J. Lett.* 553:L153
- Hansen CE, Klein RI, McKee CF, Fisher RT. 2012. *Ap. J.* 747:22
- Hartigan P, Edwards S, Ghandour L. 1995. *Ap. J.* 452:736
- Hartigan P, Kenyon SJ, Hartmann L, et al. 1991. *Ap. J.* 382:617
- Hartmann L. 2003. *Ap. J.* 585:398
- Hartmann L. 2009. *Accretion Processes in Star Formation*. Cambridge, UK: Cambridge Univ. Press. 2nd ed.
- Hartmann L, Calvet N, Gullbring E, D'Alessio P. 1998. *Ap. J.* 495:385
- Hartmann L, Cassen P, Kenyon SJ. 1997. *Ap. J.* 475:770
- Hartmann L, Hewett R, Calvet N. 1994. *Ap. J.* 426:669
- Hartmann L, Kenyon SJ. 1996. *Annu. Rev. Astron. Astrophys.* 34:207
- Hartmann L, Zhu Z, Calvet N. 2011. arXiv:1106.3343 [astro-ph.SR]

- Hayashi MR, Shibata K, Matsumoto R. 1996. *Ap. J. Lett.* 468:L37
- Herbig GH. 1977. *Ap. J.* 217:693
- Herbig GH. 1989. In *ESO Workshop on Low Mass Star Formation and Pre-Main Sequence Objects, Garching bei München, 11–13 July 1989*, ed. B Reipurth, pp. 233–46. Garching bei München, Ger: Eur. South. Obs.
- Herbig GH. 1990. *Astron. J.* 360:639
- Herbig GH. 2008. *Astron. J.* 135:637
- Herbst W, Herbst DK, Grossman EJ, Weinstein D. 1994. *Astron. J.* 108:1906
- Herczeg GJ, Cruz KL, Hillenbrand LA. 2009. *Ap. J.* 1094:529
- Herczeg GJ, Hillenbrand LA. 2008. *Ap. J.* 681:594
- Hernández J, Calvet N, Briceño C, et al. 2007. *Ap. J.* 671:1784
- Hillenbrand LA, Findeisen KP. 2015. *Ap. J.* 808:68
- Hillenbrand LA, Miller AA, Covey KR, et al. 2013. *Astron. J.* 145:59
- Holoien TWS, Prieto JL, Stanek KZ, et al. 2014. *Ap. J.* 785:L35
- Hosokawa T, Offner SSR, Krumholz MR. 2011. *Ap. J.* 738:140
- Hubrig S, Ilyin I, Schöller M, Lo Curto G. 2013. *Astron. Nachr.* 334:1093
- Hussain GAJ, Alecian E. 2014. In *Magnetic Fields Throughout Stellar Evolution: Proc. Symp. Int. Astron. Union, 302nd, Biarritz, Fr., Aug. 25–30, 2013*, ed. P Petit, M Jardine, H Spruit, pp. 25–37. Cambridge, UK: Cambridge Univ. Press
- Hussain GAJ, Collier Cameron A, Jardine MM, et al. 2009. *MNRAS* 398:189
- Ilee JD, Fairlamb J, Oudmaijer RD, et al. 2014. *MNRAS* 445:3723
- Ingleby L, Calvet N, Bergin E, et al. 2009. *Ap. J.* 703:L137
- Ingleby L, Calvet N, Bergin E, et al. 2011. *Ap. J.* 743:105
- Ingleby L, Calvet N, Herczeg GJ, et al. 2013. *Ap. J.* 767:112
- Ingleby L, Calvet N, Hernández J, et al. 2014. *Ap. J.* 790:47
- Ingleby L, Espaillat C, Calvet N, et al. 2015. *Ap. J.* 805:149
- Joergens V, Bonnefoy M, Liu Y, et al. 2013. *Astron. Astrophys.* 558:L7
- Johns-Krull CM. 2007. *Ap. J.* 664:975
- Johns-Krull CM, Chen W, Valenti JA, et al. 2013. *Ap. J.* 765:11
- Johns-Krull CM, Herczeg GJ. 2007. *Ap. J.* 655:345
- Johnstone CP, Jardine M, Gregory SG, et al. 2014. *MNRAS* 437:3202
- Jones AFAL. 2008. *Cent. Bur. Electron. Electr.* 1217:1
- Joy AH. 1945. *Ap. J.* 102:168
- Juhász A, Dullemond CP, van Boekel R, et al. 2012. *Ap. J.* 744:118
- Kalari VM, Vink JS. 2015. *Ap. J.* 800:113
- Kalari VM, Vink JS, Drew JE, et al. 2015. *MNRAS* 453:1026
- Kastner JH, Huenemoerder DP, Schulz NS, et al. 2002. *Ap. J.* 567:434
- Kenyon SJ, Gomez M, Marzke RO, Hartmann L. 1994. *Astron. J.* 108:251
- Kenyon SJ, Hartmann L, Strom KM, Strom SE. 1990. *Astron. J.* 99:869
- Kim KH, Watson DM, Manoj P, et al. 2009. *Ap. J.* 700:1017
- Kley W, Nelson RP. 2012. *Annu. Rev. Astron. Astrophys.* 50:211
- Königl A. 1989. *Ap. J.* 342:208
- Königl A. 1991. *Ap. J. Lett.* 370:L39
- Königl A, Salmeron R, Wardle M. 2010. *MNRAS* 401:479
- Kóspál A, Ábrahám P, Goto M, et al. 2011. *Ap. J.* 736:72
- Kóspál A, Ábrahám P, Prusti T, et al. 2007. *Astron. Astrophys.* 470:211
- Kóspál A, Németh P, Ábrahám P, et al. 2008. *Inf. Bull. Var. Stars* 5819:1
- Kratter K, Lodato G. 2016. *Annu. Rev. Astron. Astrophys.* 54:271–311
- Kraus S, Hofmann KH, Benisty M, et al. 2008. *Astron. Astrophys.* 489:1157
- Kun M, Apai D, O’Linger-Luscusk J, et al. 2014. *Ap. J.* 795:L26
- Kunz MW. 2008. *MNRAS* 385:1494
- Kurosawa R, Romanova MM. 2012. *MNRAS* 426:2901
- Kurosawa R, Romanova MM. 2013. *MNRAS* 431:2673
- Kurosawa R, Romanova MM, Harries TJ. 2011. *MNRAS* 416:2623

- Kwan J, Edwards S, Fischer W. 2007. *Ap. J.* 657:897
- Larson RB. 1969. *MNRAS* 145:271
- Larson RB. 1972. *MNRAS* 157:121
- Lamzin SA. 1995a. *Astrophys. Space Sci.* 224:211
- Lamzin SA. 1995b. *Astron. Astrophys.* 295:L20
- Lamzin SA. 1998. *Astron. Rep.* 42:322
- Lamzin SA. 2003. *Astron. Rep.* 47:540
- Lesur G, Kunz MW, Fromang S. 2014. *Astron. Astrophys.* 566:56
- Li ZY, Banerjee R, Pudritz RE, et al. 2014. See Beuther et al. 2014, pp. 173–94
- Lima GHRA, Alencar SHP, Calvet N, et al. 2010. *Astron. Astrophys.* 522:A104
- Lorenzetti D, Antonucci S, Giannini T, et al. 2012. *Ap. J.* 749:188
- Lovelace RVE, Covey KR, Lloyd JP. 2011. *Astron. J.* 141:L51
- Lovelace RVE, Romanova MM, Bisnovatyi-Kogan GS. 1995. *MNRAS* 275:244
- Manara CF, Beccari G, Da Rio N, et al. 2013. *Astron. Astrophys.* 558:114
- Manara CF, Robberto M, Da Rio N, et al. 2012. *Ap. J.* 755:154
- Manara CF, Testi L, Natta A, et al. 2014. *Astron. Astrophys.* 568:18
- Manara CF, Testi L, Natta A, Alcalá JM. 2015. *Astron. Astrophys.* 579:66
- Manara CF, Testi L, Rigliaco E, et al. 2013. *Astron. Astrophys.* 551:107
- Matt S, Pinzón G, Greene TP, Pudritz RE. 2012. *Ap. J.* 745:101
- Matt SP, Pudritz RE. 2005. *Ap. J. Lett.* 632:L135
- McClure MK, Calvet N, Espaillat C, et al. 2013. *Ap. J.* 188:75
- McClure MK, Furlan E, Manoj P, et al. 2010. *Ap. J. Suppl.* 188:75
- McGinnis PT, Alencar SHP, Guimarães MM, et al. 2015. *Astron. Astrophys.* 577:11
- McKee CF, Offner SSR. 2010. *Ap. J.* 716:167
- McLaughlin DB. 1946. *Astron. J.* 52:109
- Mendigutia I, Brittain S, Eiroa C, et al. 2013. *Ap. J.* 776:44
- Mendigutia I, Calvet N, Montesinos B, et al. 2011. *Astron. Astrophys.* 535:99
- Merin B, Brown JM, Oliveira I, et al. 2010. *Ap. J.* 718:1200
- Miller AA, Hillenbrand LA, Covey KR, et al. 2011. *Ap. J.* 730:80
- Mohanty S, Jayawardhana R, Basri G. 2005. *Ap. J.* 626:498
- Mottram JC, van Dishoeck EF, Schmalzl M, et al. 2013. *Astron. Astrophys.* 558:A126
- Murillo NM, Lai SP, Bruderer S, et al. 2013. *Astron. Astrophys.* 560:103
- Muzerolle J, Calvet N, Briceño C, et al. 2000. *Ap. J.* 535:L47
- Muzerolle J, Calvet N, Hartmann L. 2001. *Ap. J.* 550:944
- Muzerolle J, D'Alessio P, Calvet N, Hartmann L. 2004. *Ap. J.* 617:406
- Muzerolle J, Hartmann L, Calvet N. 1998. *Astron. J.* 116:2965
- Muzerolle J, Hillenbrand L, Calvet N, et al. 2003. *Ap. J.* 592:266
- Muzerolle J, Luhman KL, Briceño C, et al. 2005. *Ap. J.* 625:906
- Myers PC. 2011. *Ap. J.* 743:98
- Myers PC. 2014. *Ap. J.* 781:33
- Najita JR, Andrews SM, Muzerolle J. 2015. *MNRAS* 450:3559
- Najita JR, Carr JS, Mathieu RD. 2003. *Ap. J.* 589:931
- Najita JR, Strom SE, Muzerolle J. 2007. *MNRAS* 378:369
- Natta A, Testi L, Alcalá JM, et al. 2014. *Astron. Astrophys.* 569:5
- Natta A, Testi L, Muzerolle J, et al. 2004. *Astron. Astrophys.* 424:603
- Natta A, Testi L, Randich S. 2006. *Astron. Astrophys.* 452:245
- Nguyen DC, Scholz A, van Kerkwijk MH, et al. 2009. *Ap. J.* 694:L153
- Nisini B, Antonucci S, Giannini T, Lorenzetti D. 2005. *Astron. Astrophys.* 429:543
- Offner SSR, McKee CF. 2011. *Ap. J.* 736:53
- Ohashi N, Saigo K, Aso Y, et al. 2014. *Ap. J.* 796:131
- Orlando S, Sacco GG, Argiroffi C, et al. 2010. *Astron. Astrophys.* 510:A71
- Oudmaijer RD, van den Ancker ME, Baines D, et al. 2011. *Astron. Nacht.* 332:238
- Owen JE, Clarke CJ, Ercolano B. 2012. *MNRAS* 422:1880

- Owen JE, Ercolano B, Clarke CJ. 2011. *MNRAS* 412:13
- Padoan P, Haugbølle T, Nordlund Å. 2014. *Ap. J.* 797:32
- Palla F, Stahler SW. 1991. *Ap. J.* 375:288
- Palla F, Stahler SW. 1999. *Ap. J.* 525:772
- Pascucci I, Gorti U, Hollenbach D, et al. 2006. *Ap. J.* 651:1177
- Perez-Becker D, Chiang E. 2011. *Ap. J.* 735:8
- Petrov PP, Gahm GF, Herczeg GH, et al. 2014. *Astron. Astrophys.* 568:L10
- Petrov PP, Gahm GF, Stempels HC, et al. 2011. *Astron. Astrophys.* 535:6
- Popham R, Kenyon S, Hartmann L, Narayan R. 1996. *Ap. J.* 473:422
- Pudritz RE, Norman CA. 1983. *Ap. J.* 274:677
- Rigliaco E, Natta A, Randich S, et al. 2011. *Astron. Astrophys.* 526:L6
- Rigliaco E, Natta A, Testi L, et al. 2012. *Astron. Astrophys.* 548:56
- Rigliaco E, Pascucci I, Duchene G, et al. 2015. *Ap. J.* 801:31
- Rigliaco E, Pascucci I, Gorti U, et al. 2013. *Ap. J.* 772:60
- Robberto M, Song J, Mora Carrillo G, et al. 2004. *Ap. J.* 606:952
- Romanova MM, Kulkarni AK, Lovelace RV. 2008. *Ap. J. Lett.* 673:L171
- Romanova MM, Long M, Lamb FK, et al. 2011. *MNRAS* 411:915
- Romanova MM, Lovelace RVE, Bachetti M, et al. 2014. *Eur. Phys. J. Web Conf.* 64:05001
- Romanova MM, Ustyugova GV, Koldoba AV, Lovelace RVE. 2004. *Ap. J.* 610:920
- Romanova MM, Ustyugova GV, Koldoba AV, Lovelace RVE. 2012. *MNRAS* 421:63
- Rucinski SM, Matthews JM, Kuschnig R, et al. 2008. *MNRAS* 391:1913
- Sacco GG, Argiroffi C, Orlando S, et al. 2008. *Astron. Astrophys.* 491:L17
- Sacco GG, Orlando S, Argiroffi C, et al. 2010. *Astron. Astrophys.* 522:A55
- Safron EJ, Fischer WJ, Megeath ST, et al. 2015. *Ap. J. Lett.* 800:L5
- Salyk C, Blake G, Boogert ACA, Brown JM. 2011. *Ap. J.* 743:112
- Salyk C, Herczeg GJ, Brown JM, et al. 2013. *Ap. J.* 769:21
- Schönke J, Tscharnuter WM. 2011. *Astron. Astrophys.* 526:A139
- Shu FH. 1977. *Ap. J.* 214:488
- Shu FH, Lizano S, Ruden SP, Najita J. 1988. *Ap. J. Lett.* 328:L19
- Sicilia-Aguilar A, Fang M, Roccatagliata V, et al. 2015. *Astron. Astrophys.* 580:82
- Sicilia-Aguilar A, Henning Th, Hartmann L. 2010. *Ap. J.* 710:597
- Sicilia-Aguilar A, Kóspál A, Setiawan J, et al. 2012. *Astron. Astrophys.* 544:93
- Simon JB, Lesur G, Kunz MW, Armitage PJ. 2015. *MNRAS* 454:1117
- Siwak M, Rucinski SM, Matthews JM, et al. 2011. *MNRAS* 415:1119
- Soderblom DR. 2010. *Annu. Rev. Astron. Astrophys.* 48:581
- Soderblom DR, Hillenbrand LA, Jeffries RD, et al. 2014. See Beuther et al. 2014, pp. 219–41
- Sousa A, Alencar SHP, Bouvier J, et al. 2016. *Astron. Astrophys.* 586:A47
- Stahler SW. 1988. *Ap. J.* 332:804
- Stahler SW, Shu FH, Taam RE. 1980. *Ap. J.* 241:637
- Stauffer J, Cody AM, Baglin A, et al. 2014. *Astron. J.* 147:83
- Stelzer B, Micela G, Hamaguchi K, Schmitt JHMM. 2006. *Astron. Astrophys.* 457:223
- Stelzer B, Schmitt JHMM. 2004. *Astron. Astrophys.* 418:687
- Symington NH, Harries TJ, Kurosawa R, Naylor T. 2005. *MNRAS* 358:977
- Terebey S, Shu FH, Cassen P. 1984. *Ap. J.* 286:529
- Tobin JJ, Hartmann L, Chiang HF, et al. 2012. *Nature* 492:83
- Turner NJ, Fromang S, Gammie C, et al. 2014. See Beuther et al. 2014, pp. 411–32
- Valenti JA, Basri G, Johns CM. 1993. *Ap. J.* 106:2024
- van der Marel N, van Dishoeck EF, Bruderer S, et al. 2015. *Astron. Astrophys.* 579:A106
- van der Marel N, van Dishoeck EF, Bruderer S, et al. 2016. *Astron. Astrophys.* 585:58
- van Kempen TA, van Dishoeck EF, Salter DM, et al. 2009. *Astron. Astrophys.* 498:167
- Vaytet N, Chabrier G, Audit E, et al. 2013. *Astron. Astrophys.* 557:A90
- Venuti L, Bouvier J, Flaccomio E, et al. 2014. *Astron. Astrophys.* 570:82
- Venuti L, Bouvier J, Irwin J, et al. 2015. *Astron. Astrophys.* 581:66

- Vink JS, Drew JE, Harries TJ, Oudmaijer RD. 2002. *MNRAS* 337:356
- Vorobyov EI, Basu S. 2005. *Ap. J. Lett.* 633:L137
- Vorobyov EI, Basu S. 2010. *Ap. J.* 719:1896
- Vorobyov EI, Basu S. 2015. *Ap. J.* 805:115
- Wade GA, Bagnulo S, Drouin D, et al. 2007. *MNRAS* 376:1145
- Wardle M. 1999. *MNRAS* 307:849
- Wardle M, Salmeron R. 2012. *MNRAS* 422:2737
- White RJ, Basri G. 2003. *Ap. J.* 582:1109
- White RJ, Ghez AM. 2001. *Ap. J.* 556:265
- White RJ, Greene TP, Doppmann GW, et al. 2007. In *Protostars and Planets*, Vol. 5, ed. B Reipurth, D Jewitt, K Keil, pp. 117–32. Tucson: Univ. Ariz. Press
- White RJ, Hillenbrand LA. 2004. *Ap. J.* 616:998
- Wilking BA, Lada CJ, Young ET. 1989. *Ap. J.* 340:823
- Williams JP, Cieza LA. 2011. *Annu. Rev. Astron. Astrophys.* 49:67
- Yang H, Johns-Krull CM, Valenti JA. 2007. *Ap. J.* 133:73
- Young CH, Jørgensen JK, Shirley YL, et al. 2004. *Ap. J. Suppl.* 154:396
- Zanni C, Ferreira J. 2013. *Astron. Astrophys.* 550:A99
- Zhang K, Crockett N, Salyk C, et al. 2015. *Ap. J.* 805:55
- Zhou Y, Herczeg GJ, Kraus AL, et al. 2014. *Ap. J.* 783:L17
- Zhu Z, Espaillat C, Hinkle K, et al. 2009. *Ap. J. Lett.* 694:L64
- Zhu Z, Hartmann L, Calvet N, et al. 2007. *Ap. J.* 669:483
- Zhu Z, Hartmann L, Gammie C. 2009. *Ap. J.* 694:1045
- Zhu Z, Nelson RP, Hartmann L, et al. 2011. *Ap. J.* 729:47



Contents

A Fortunate Half-Century <i>Jeremiah P. Ostriker</i>	1
The Remnant of Supernova 1987A <i>Richard McCray and Claes Fransson</i>	19
Astrophysics with Extraterrestrial Materials <i>Larry R. Nittler and Fred Ciesla</i>	53
Red Clump Stars <i>Léo Girardi</i>	95
Accretion onto Pre-Main-Sequence Stars <i>Lee Hartmann, Gregory Herczeg, and Nuria Calvet</i>	135
Interstellar Hydrides <i>Maryvonne Gerin, David A. Neufeld, and Javier R. Goicoechea</i>	181
The Quest for B Modes from Inflationary Gravitational Waves <i>Marc Kamionkowski and Ely D. Kovetz</i>	227
Gravitational Instabilities in Circumstellar Disks <i>Kaitlin Kratter and Giuseppe Lodato</i>	271
The Evolution of the Intergalactic Medium <i>Matthew McQuinn</i>	313
The Magellanic Stream: Circumnavigating the Galaxy <i>Elena D'Onghia and Andrew J. Fox</i>	363
Masses, Radii, and the Equation of State of Neutron Stars <i>Feryal Özel and Paulo Freire</i>	401
The Eccentric Kozai-Lidov Effect and Its Applications <i>Smadar Naoz</i>	441
Protostellar Outflows <i>John Bally</i>	491

The Galaxy in Context: Structural, Kinematic, and Integrated Properties <i>Joss Bland-Hawthorn and Ortwin Gerhard</i>	529
Structure and Kinematics of Early-Type Galaxies from Integral Field Spectroscopy <i>Michele Cappellari</i>	597
Six Decades of Spiral Density Wave Theory <i>Frank H. Shu</i>	667
Gamma-Ray Observations of Active Galactic Nuclei <i>Grzegorz (Greg) Madejski and Marek Sikora</i>	725
Galaxies in the First Billion Years After the Big Bang <i>Daniel P. Stark</i>	761

Indexes

Cumulative Index of Contributing Authors, Volumes 43–54	805
Cumulative Index of Article Titles, Volumes 43–54	808

Errata

An online log of corrections to *Annual Review of Astronomy and Astrophysics* articles may be found at <http://www.annualreviews.org/errata/astro>